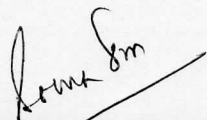# UNIVERSITY GRANTS COMMISSION
BAHADUR SHAH ZAFAR MARG
NEW DELHI – 110 002
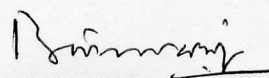
SUBMISSION OF INFORMATION AT THE TIME OF SENDING THE FINAL REPORT OF THE WORK DONE ON THE PROJECT

1.	Name and address of the Principal Investigator	**Dr. Soma Das** Department of Electronics & Communication Engineering, Guru Ghasidas Vishwavidyalaya (Central University), Bilaspur – 495009, C.G.
2.	Name and address of the Institution	Department of Electronics & Communication Engineering, Guru Ghasidas Vishwavidyalaya (Central University), Bilaspur – 495009, C.G.
3.	UGC Approval No. & Date	42-908/2013 (SR), 25-03-2013
4.	Date of Implementation	01-04-2013
5	Tenure of the Project	01-04-2013 to 31-03-2017 (4 years after extension)
6.	Total Grant Allocated	Rs. 1203300/-
7.	Total Grant Received	Rs. 1115500/-
8.	Final Expenditure	Rs. 813310/-
9.	Title of the Project	Investigation on the properties & Optimization of the materials for room temperature Magnetic Refrigeration Applications
10.	Objective of the Project	• To prepare good quality magnetic materials targeting to enhance their magnetic properties near transition temperature. • To characterize the magnetocaloric properties and the physical mechanisms associated with the magnetic degrees of freedom. • Material characterization to be done through XRD, SEM, TEM, Transport and magnetic properties. • To interpret and analyze the collected experimental data to explain and to predict the behavior of the material in the thermal cycles of the refrigeration in prototype.
11.	Whether Objectives were achieved	Promising results are achieved and are published in international journals
12.	Achievements from the Project	• A Research Laboratory has been set up with the equipment purchased through this project. • Research Publication is carried out with the results obtained from this project
13.	Summary of Findings (in 500 words)	Enclosure-I
14.	Contribution to society	The findings of this project are acceptable as a promising magnetic material that can be useful in different technological applications like spintronics, magnetic sensors, memory device etc.
15.	Whether any PhD enrolled/ produced out of the project	Nil
16.	No. of publications out of the project (reprint attached – Annexure-II)	No. of journal publication= 02 (communicated), Conference presentation =01 No. of conference presentation=01 (25th National symposium on Cryogenics, 8-10 Dec, 2014)

PRINCIPAL INVESTIGATOR
(SIGNATURES WITH SEAL)

Dr. Soma Das
Principal Investigator,
UGC Project,

REGISTRAR
(SIGNATURES WITH SEAL)
Registrar
गुरु घासीदास विश्वविद्यालय, बिलासपुर (छ.ग.)
Guru Ghasidas Vishwavidyalaya,
Bilaspur (C.G.)

SUMMARY OF REPORT

Name and address of the   Dr. Soma Das, Assistant Professor.
Principal Investigator: Department of Electronics & Communication Engineering,
Guru Ghasidas Vishwavidyalaya (Central University)
Bilaspur – 495009 (CG)
UGC Approval no. and date: 42-908/2013(SR) dated 25-03-2013
Title of the Project: Investigation on the properties & Optimization of the materials for
room temperature Magnetic Refrigeration Applications

Lanthanum-based manganite perovskites exhibiting colossal magnetoresistance (CMR) have attracted great attention in recent years. Since the ferromagnetism (FM) in manganites is correlated with the metallic properties and CMR effect, the origin of FM and the possibility to control it are of profound interest. The FM and metal-like behavior occurring in hole-doped manganites results usually from a substitution of La sites, by divalent ions such as Sr^{2+}, in the undoped parent compound $LaMnO_3$. Self-doped lanthanum manganite $La_{1-x}MnO_3$ exhibit magnetic and electrical transport properties very similar to the hole doped manganites where Mn^{4+} appears due to the self-doping, analogous to the hole doping, leading to the spectacular changes in the physical properties. The relative amount of Mn^{3+}/Mn^{4+} ratio and their distribution in the lattice as well as the nonstoichiometric oxygen (creating the equivalent vacancies in La and Mn-sites) plays an important role in tuning the physical properties of these systems.

Until now, no comparative studies have been carried out on cation-deficiencies of $LaMnO_3$ in terms of both the substitution of La by a divalent ion and creating La-deficiency. In this work, we have studied the structure, electric and magnetic properties of cation-deficient compositions with creating vacancies in La-site or/and substitution of La-site by a Sr ($\leq 10\%$). We have studied two types of samples. One type was prepared by Sr doping (degree of Sr doping = 10%, 5%, 0%) on self-deificient La-site and another one with Sr doping (degree of Sr doping= 5%) on La-site of stoichometric compound, $LaMnO_3$, resulting the variation of Mn^{4+} concentration of both type of samples.

The single phase of compounds was confirmed by the powder X-ray diffraction (Seifert XRD 3000 P) using $CuK\alpha$ radiation. The size and morphology of the grains of the samples were observed in a JEOL JSM 35 C scanning electron microscope (SEM). Oxygen non-stoichiometry for all samples were checked through iodometric titration as the average of 5 titration values giving the excess oxygen $\approx 1.5\%$. The resistivity and MR were measured by the standard four-probe technique in an electromagnet and a commercial closed cycle refrigerator operating down to 10 K (Janis Research Inc.). All the thermal variation during resistivity measurements was carried out at a fixed rate of 2 K/min. DC Magnetization was measured in vibrating sample magnetometer (VSM) with a field range from 0 to 10 T. In case of zero-field cooled (ZFC) mode the sample was cooled down to the desired temperature at zero magnetic field while for the field-cooled (FC) mode the sample was cooled in a static magnetic field.

The low temperature metallic behavior with a characteristic feature of metal to semiconducting transition accompanying with a typical feature of FM character are observed for the samples. The compound with Sr−5% shows different characteristic features such as two FM ordering temperatures at T_{C1} and T_{C2} (detailed in paper), absence of sharp peak at Tp in $\rho(T)$, and linear ohmic I − V behavior below T_C. Increasing Mn^{4+} content with Sr content as well as La deficiency commits the hole-rich FM and metallic phases. The distinct behavior of low field MR below T_C is suggested due to the tunneling of electrical transport across the GB region. The analysis of the nonlinear current-voltage curves for La deficient samples further indicates that the inelastic tunneling via localized states of the GB region is dominant.

FINAL PROJECT REPORT

i. Brief objective of the project

The objective of the project is to develop a good magnetic refrigerant system and to understand the dynamics of the system in the real-state environment of a room temperature magnetic refrigerator. Since magnetic refrigeration is an important cooling technology regarding its environment-friendly processing and the executable high efficiency compared to the conventional gas-refrigeration one, interest has been given to solve the problems and challenges of this technology specially for the room temperature applications.

The objective therefore is to prepare good quality materials targeting to enhance their magnetic properties near transition temperature. Then will be the study of their properties relevant to characterize the magnetocaloric properties and the physical mechanisms associated with the magnetic degrees of freedom. The characterization of the materials will also be done accordingly. After collecting the experimental data, the objective will be to interpret and analyze the data in explaining and predicting the behavior of the material in the thermal cycles of the refrigeration in prototype. Effort will be given to model the thermomagnetic response of the system in prototype magnetocaloric devices.

ii. Introduction

Lanthanum-based manganite perovskites exhibiting colossal magnetoresistance (CMR) have attracted great attention in recent years [1,2]. The presence of Mn^{3+} and Mn^{4+} ions together with the site-site double-exchange (DE) mechanism [3] play pivotal role towards such CMR effect. Since in manganites the ferromagnetism (FM) is correlated with the metallic properties and CMR effect, the origin of FM and the possibility to control it are of profound interest. The FM and metal-like behavior observed in hole-doped manganites results usually from a substitution of La sites, by divalent ions such as Sr^{2+}, in the undoped parent compound $LaMnO_3$ [4–6]. Self-doped lanthanum manganite $La_{1-x}MnO_3$ exhibits magnetic and electrical transport properties very similar to the hole doped manganites where Mn^{4+} appears due to the self-doping [7–11]. Similar to the hole doping, variation of Mn^{4+} leading to the spectacular changes in the physical properties of selfdoped lanthanum manganite. The amount of Mn^{3+}/Mn^{4+} ratio and their distribution in the lattice as well as the nonstoichiometric oxygen (creating the equivalent vacancies in La and Mn-sites) plays an important role in tuning the physical properties of these compounds. For low-doped compositions, the superexchange interaction between the Mn^{3+} ions is responsible for the appearance of FM and/or antiferromagnetic (AFM) insulating phases. The Jahn-Teller (JT) coupling plays an important role leading to the orbital ordering of Mn^{3+} ions and determining also the sign of exchange coupling in accordance with degree of static deformation of the MnO_6 octahedra [12]. The magnetic phase separation occurs with increasing doping, as a result of competition between different kinds of interactions in the system, leading to a mixed AFM-FM ground state. The existence of Mn^{4+} can be achieved by both the substitution of La by a divalent ion as well as creating La-deficiency [13,14]. These changes give evidence of direct correlation among magnetic, structural and electrical properties; namely,

the magnetic behavior of the system. This magnetic behavior evolves from AFM to FM with a reduction of JT distortion in the MnO_6 sublattice when structural symmetry changes from the orthorhombic to the rhombohedral [15–18], and when an electron is allowed to hop between Mn^{3+} and Mn^{4+} ions producing a ferromagnetic DE interaction [3], which also promotes a metallic electric conduction.

Until now, no comparative studies have been carried out on cation deficiencies of $LaMnO_3$ in terms of both the substitution of La by a divalent ion and creating La-deficiency. We have studied two types of samples: one type was prepared by Sr doping (degree of Sr doping=10%, 5%, 0%) on self-deificient La-site and another one with Sr doping (degree of Sr doping=5%) on La-site of stoichometric compound, $LaMnO_3$, resulting the variation of Mn^{4+} concentration of both type of samples. In the present paper, we are going to focus on the evolution of structural, electrical and magnetic properties with the changes in the Mn^{4+} concentration in cation-deficient compounds by creating vacancies in La-site and/or substitution of La-site by a Sr (≤10%).

iii. Methodology adopted for this work

The methodology adopted for this work is as given below:

i. We have already prepared good quality materials starting with oxide perovskites in nano-sizes of certain composition to get a room temperature transition with good magnetic moment.

ii. We have adopted different conditions of heat treatment processes to analyse the changes in micro-structure and related changes in their magnetic and transport properties.

iii. XRD/SEM/TEM structural studies to characterize the samples.

iv. Physical properties as dc resistivity, magnetoresistance, detailed magnetic measurements by VSM and SQUID, thermal expansion and specific heat.

v. Study of the dynamic thermal and magnetic responses of the magnetic materials with respect to changes of magnetic field, in conditions relevant for the application in the thermal cycles of the refrigeration in a prototype.

vi. Theoretical interpretation of the result by appropriate modeling of magnetocaloric effects, in second-order and first-order magnetic transition materials (reduction of hysteresis).

vii. Modeling of thermomagnetic response.

iv. Experimental Details

Polycrystalline compounds of nominal composition (a) $[La_{0.9}Sr_{0.1}]_{0.9}MnO_3$, (b) $[La_{0.95}Sr_{0.05}]_{0.9}MnO_3$, (c) $La_{0.9}MnO_3$ and (d) $La_{0.95}Sr_{0.05}MnO_3$ were prepared by the chemical route [19,20]. The final heat treatment was performed at 800 °C for 15 h in air, followed by furnace cooling to room temperature. In order to remove the ambiguity ascribed to the different oxygen nonstoichiometry, the sample was finally annealed under close oxygen atmosphere for 6 h at 1000 °C. Henceforth, we will refer the samples, denoted with La-site deficiency, by their respective degree of Sr substitution on La-site such as $[La_{0.9}Sr_{0.1}]_{0.9}MnO_3$ as DSr–10%, $[La_{0.95}Sr_{0.05}]_{0.9}MnO_3$ as DSr–5% and $La_{0.9}MnO_3$ as DSr–0%, and the remaining La-stoichiometric compound $La_{0.95}Sr_{0.05}MnO_3$ will be designated by only the respective degree

of Sr substitution as Sr–5%. The single phase of compounds was confirmed by the powder X-ray diffraction (Seifert XRD 3000 P) using CuKα radiation. The size and morphology of the grains of the samples were observed in a JEOL JSM 35 C scanning electron microscope (SEM). Oxygen nonstoichiometry for all samples was checked through iodometric titration as the average of 5 titration values giving the excess oxygen ≈1.5%. The resistivity (ρ) and MR were measured by the standard four-probe technique in an electromagnet and a commercial closed cycle refrigerator operating down to 10 K (Janis Research Inc.). All the thermal variation during resistivity measurements was carried out at a fixed rate of 2 K/min. DC Magnetization was measured in vibrating sample magnetometer (VSM) with a field range from 0 to 10 T. In case of zero-fieldcooled (ZFC) mode the sample was cooled down to the desired temperature at zero magnetic field while for the field-cooled (FC) mode the sample was cooled in a static magnetic field.

v. Detailed Results & Discussions

SEM images of studied compounds DSr–10%, DSr–5%, DSr–0% and Sr–5% are shown in Fig. 1(a)-(d), respectively, which clearly show melted grain boundaries. The grains exhibit inhomogeneity in size with average diameter ≈170, ≈160, ≈230 and≈120 nm for the compounds DSr−10%, DSr−5%, DSr−0% and Sr−5%, respectively.
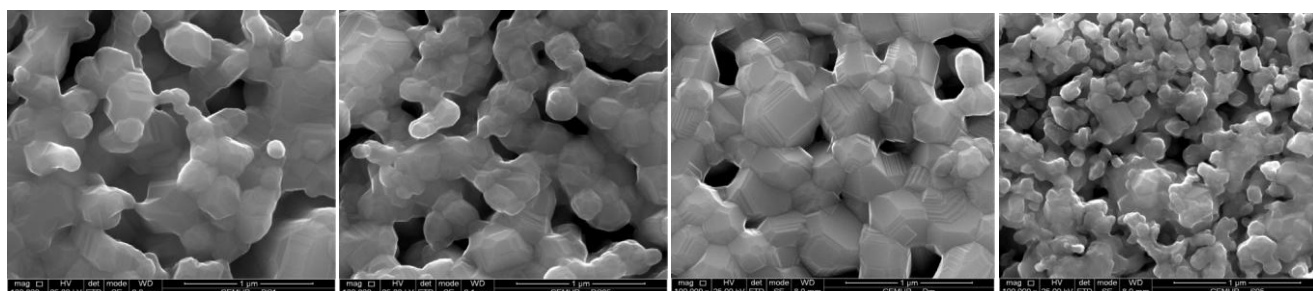

Fig. 1. SEM image of (a) DSr–10% (b) DSr–5% (c) DSr–0% and (d) Sr–5%.

Table 1
Some selected refined structural parameters Obtained from the Rietveld Refinement of the Room Temperature Structure of compounds $DSr − 10\%$, $DSr − 5\%$, $DSr − 0\%$ and $Sr − 5\%$.

Parameters	rhombohedral, $R\bar{3}c$			
	$DSr − 10\%$	$DSr − 5\%$	$DSr − 0\%$	$Sr − 5\%$
a (Å)	5.518(3)	5.515(3)	5.522(2)	5.513(4)
c (Å)	13.367(5)	13.358(2)	13.357(6)	13.336(2)
V (Å^3)	352.53(6)	351.92(8)	352.76(8)	351.07(7)
χ^2	2.440(1)	2.683(6)	2.568(8)	2.266(6)
Mn−O (Å^2)	1.944(1)	1.945(6)	1.952(6)	1.941(3)
Mn−O−Mn (deg)	178.51(5)	173.76(8)	169.43(3)	178.51(4)
Mn−Mn (Å)	3.887(7)	3.885(5)	3.888(6)	3.882(4)

The crystal structure of the systems were analyzed by Rietveld refinement (using the MAUD software package) of XRD data. The Rietveld analysis show that these compounds form in a single phase rhombohedral symmetry with space group $R\bar{3}c$. The refinement was also performed in considering

orthorhombic symmetry with space group *Pnma*. However, the agreement factor, χ^2 was significantly improved (Table 1) when rhombohedral symmetry with space group $R\bar{3}c$ was introduced. This structural analysis is in support of the undoped mother sample LaMnO$_3$ [19]. Fig. 2 displays Rietveld fitted XRD patterns of four compounds DSr−10%, DSr−5%, DSr−0% and Sr−5%, respectively. The selected refined structural parameters and agreement factors are given in Table 1. We did not observe any systematic change of lattice parameters and unit cell volumes with variation of Sr-concentration. Merely, lattice parameter 'c' decreases systematically with Sr-concentration for La-deficient samples. It is also observed that the Mn-O-Mn bond angle decreases with Sr-concentration except stoichemetric sample (Sr–5%). However, the variation of bond angle is understood by considering the valence state of Mn ion. The percentage of Mn^{3+} ion increases with decreasing Sr^{2+} in La-defficient samples to neutralized the charge. Progressively, the larger Mn^{3+} ions replace smaller Mn^{4+} ions, shearing corners in MnO$_6$ octahedra resulting the decrease in average Mn-O-Mn bond angle. Such peculiar change in bond angle is also observed earlier in manganites [21–23].
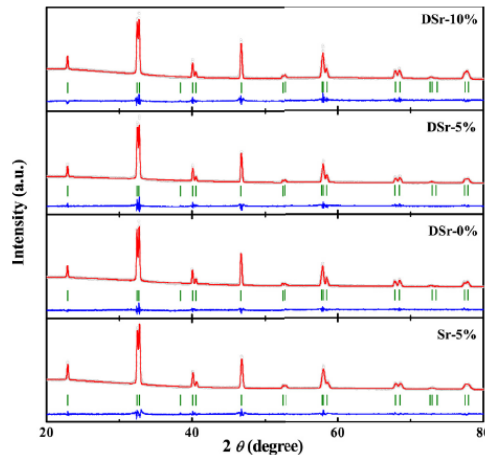

Fig. 2. Experimentally observed (dots), Rietveld calculated (continuous line), and their difference (continuous bottom line) profiles for DSr–10%, DSr–5%, DSr–0% and Sr–5% at room temperature obtained after Rietveld analysis of the XRD data using rhombohedral space group $R\bar{3}c$. The vertical tick marks between the observed and difference plots show the Bragg peak positions.
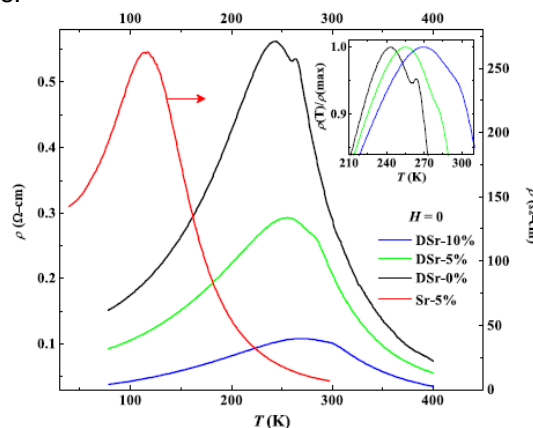

Fig. 3. Temperature dependence of resistivity (ρ) in zero field for DSr–10%, DSr–5%, DSr–0% and Sr–5%. The inset exhibits the temperature dependence of ρ(T)/ρ(max) in a selective temperature region.

The temperature variation of resistivity (ρ) in zero field is shown in Fig. 3 for the compounds DSr − 10%, DSr − 5%, DSr − 0% and Sr −5%, respectively. All the four compounds exhibit insulator-metal (I-M) transition at different temperature region. In comparison to pure $LaMnO_3$, the resistivity is decreased by an order of 3 (i.e. from KΩ-cm to Ω-cm) for all the doped samples [19]. Also the metal-insulator transition temperature which was absent in $LaMnO_3$ [19], now appears in all the four doped samples as seen in Fig. 3. The Mn^{4+} concentration (Table 2) for all compounds has strong effect in their $\rho(T)$ data, which is clearly visible from Fig. 3. A broad maximum appeared around 115 K (Tm) for Sr–5%. The different $\rho(T)$ behavior of Sr–5% has been explained in our previous report [24,25]. On the other hand, a sharp peak is observed at 264 K (Tp) accompanied by a broad maximum around$\approx$243 K (Tm) for DSr–0% (inset of Fig. 3). The features of $\rho(T)$ for DSr–0% is consistent with the previous result where the Tp is 4 K higher than the reported result [9,10,26]. The similar temperature dependence of ρ is also noticed for DSr − 5% and DSr − 10%. Inset of Fig. 3 shows that the sharp peak at Tp becomes less prominent and shifts towards higher temperature at Tp=280 and 293 K for DSr − 5% and DSr − 10%, respectively. In addition with Tp, the width of broad maximum increases with increasing Sr-concentration and Tm is noticed $\approx$255 and$\approx$263 K for DSr−5% and DSr−10%, respectively. The appearance of a sharp peak (Tp) and a broad maximum (Tm) is attributed to the inhomogeneity of the oxygen stoichiometry in different phases in the samples, where the oxygen-rich phase is responsible for the appearance of sharp peak in $\rho(T)$ [9,10,26]. It is interesting to note that the increase of Mn^{4+} concentration leads to a metal like temperature dependence ($d\rho/dT \geq 0$) and the absolute value of ρ at 400 K ($\rho400K$) decreases with increasing Mn^{4+} percentage for all samples which is listed in Table 2. As a result of La deficiency in DSr − 0%, the onset oxidation state of Mn changes from Mn^{3+} to 30% Mn^{4+}. Furthermore, Sr^{2+} substitution implants more Mn^{4+} in the Mn^{3+} matrix. Both La deficiency as well as doping divalent Sr onto the trivalent La sites results in hole doping (Mn^{4+}) and the eventual onset of metallic behavior. The percentage of Mn^{4+} of all samples is shown in Table 2. It is widely accepted [27,28] that the current carriers in hole doped ($La_{1-x}A_xMnO_3$) and self doped ($La_{1-\delta}MnO_3$) manganites, at least at moderate x and δ, are mobile holes, which appear due to charge compensation and move from Mn^{4+} ions to normal-valence Mn^{3+} ions. These holes simultaneously dominate the metallic transport and mediate the FM double-exchange (DE) interaction.

Fig. 4 shows the temperature (T) dependence of magnetization (M) measured at 100 Oe in ZFC and FC protocols for DSr–10%, DSr–5%, DSr–0% and Sr–5%. The compounds DSr − 10%, DSr − 5%, DSr − 0% show typical ferromagnetic behavior. However, for stoichemetric compound Sr − 5%, the M − T behavior is quite different. The distinct magnetic response of Sr − 5% was explained by an unusual ferromagnetic ordering which dominated this system over a wide temperature range as reported previously [24,25]. The Sr-concentrations on La-deficient samples are found to affect magnetic behavior. A sharp ferromagnetic transition is observed for all La-deficient samples. Large thermomagnetic irreversibility between ZFC and FC data below TC in Fig. 4 arises either from the magnetic anisotropy [29] or due to spin-glass-like behavior [30]. The magnetization curves at 5 K in Fig. 5 exhibit soft ferromagnetic features for all La-deficient compounds and thus the possibility of spin-glass-like feature has been ruled out. A sharp PM to FM transition is observed at T_C, as obtained from the deep in the plot

of temperature derivation of FC magnetization (dM_{FC}/dT) with T, where M_{FC} is the FC magnetization. T_C for all the compounds is shown in Table 2. In comparison to LaMnO$_3$, T_C increase closed to room temperature approximately from 140 K (for LaMnO$_3$) [19].

Table 2

Mn^{+4} (%); Sharp maximum in $\rho(T)$, (T_p); Broad maximum in $\rho(T)$, (T_m); Curie temperature (T_C); Curie–Weiss temperature (Θ_W); Effective magnetic moment from the Curie–Weiss plot (μ_{eff}); Theoretical effective magnetic moment (μ_{eff}^{th}); Saturation magnetic moment at 5 K (μ_{sat}); Theoretical Saturation moment (μ_{sat}^{th}) for compounds DSr–10%, DSr–5%, DSr–0% and Sr–5%.

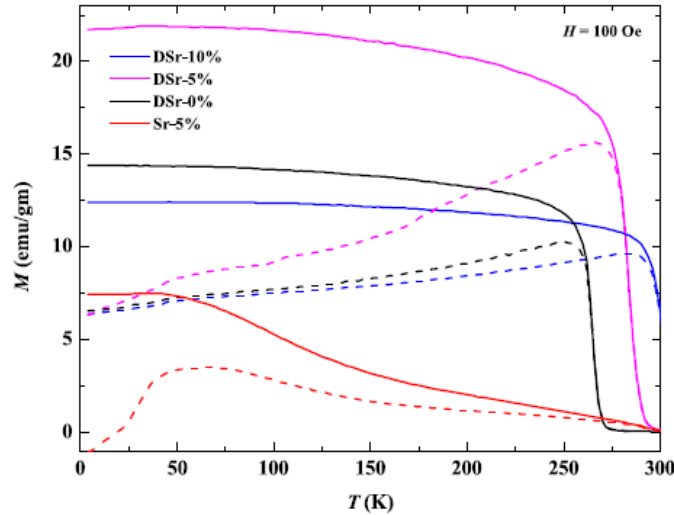| Sample	DSr–10%	DSr–5%	DSr–0%	Sr–5%
Mn^{+4} (%)	39	33.5	30	5
T_p (K)	293	280	264	–
T_m (K)	263	255	243	115
ρ_{400K} (Ω–cm)	0.035	0.056	0.074	0.144
T_C (K)	303	290	265	T_{C1} = 290 K T_{C2} = 150 K
Θ_W (K)	303	290	265	283
μ_{eff} (μ_B/f.u.)	4.85	4.83	4.80	3.25
μ_{eff}^{th} (μ_B/f.u.)	4.53	4.57	4.61	4.85
μ_{sat} (μ_B/f.u.)	3.65	3.83	3.69	2.91
μ_{sat}^{th} (μ_B/f.u.)	3.64	3.68	3.71	3.95

Fig. 4. Temperature dependence of ZFC (dotted lines) and FC (solid lines) magnetization in an applied field of 100 Oe for DSr–10%, DSr–5%, DSr–0% and Sr–5%.
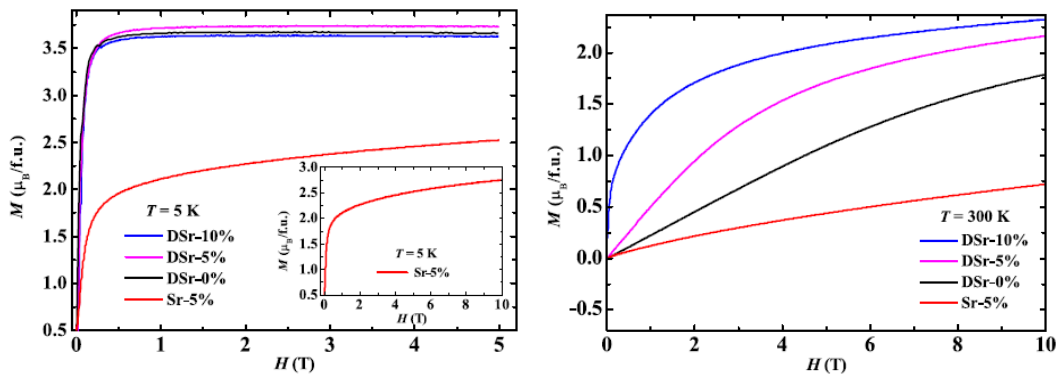

Fig. 5. Magnetization as a function of applied field for DSr − 10%, DSr − 5%, DSr−0% and Sr−5% measured at different temperatures. The inset of the left panel exhibits the extended view of the same for Sr − 5% at 5 K up to 10 T.

8

We have examined the plot of inverse susceptibility (H/M) with temperature which follows a linear behavior above T_C, in the measured range up to 330 K, according to the Curie-Weiss law: $M/H = C/(T-\Theta_W)$, where C and Θ_W are the Curie and Weiss constant, respectively. The obtained value of the effective paramagnetic moment (μ_{eff}) and ΘW are shown in Table 2. The value of Θ_W is in good agreement with Curie temperature (T_C) for all the samples. The values of μ_{eff} can be compared to that obtained from the theoretical model [31,32]. Considering the rigid Hund coupling within Mn^{3+} and Mn^{4+} in their high spin state, the theoretical effective paramagnetic moment (μ_{eff}^{th}) per formula unit can be estimated and listed in Table 2. Note that the value of μ_{eff} for all La deficient samples (DSr–10%, DSr–5%, DSr–0%) is about ≈10% larger than the theoretical provided values while that for Sr–5% is ≈15% lower than it. Considering the presence of almost same amount of excess oxygen (less than 2%) in these compounds, the larger value of μ_{eff} in La deficient samples indicates a probable existence of FM cluster [7,8,19]. The presence of surface disordered effect at the grains and/or magnetic clustering counts for lower value of μ_{eff} for Sr − 5% [24,25]. It is worth to note that the large value of μ_{eff} (6.07 μ_B/f.u.) for pure $LaMnO_3$ compared to the spin only value for S = 2 (4.90 μ_B/f.u.) suggests the existence of superparamagnetic clusters, where the inside interaction is ferromagnetic [19]. With increasing Mn^{4+} content the value of T_C shifted towards higher temperature. T_C for DSr − 0% was estimated at 265 K which coincides the value of Tp in temperature dependence of ρ. It is understood that increasing Mn^{4+} content with Sr content as well as La deficiency commits the hole-rich ferromagnetic phases dominated by the ferromagnetic double exchange interaction between Mn^{4+} and Mn^{3+}.
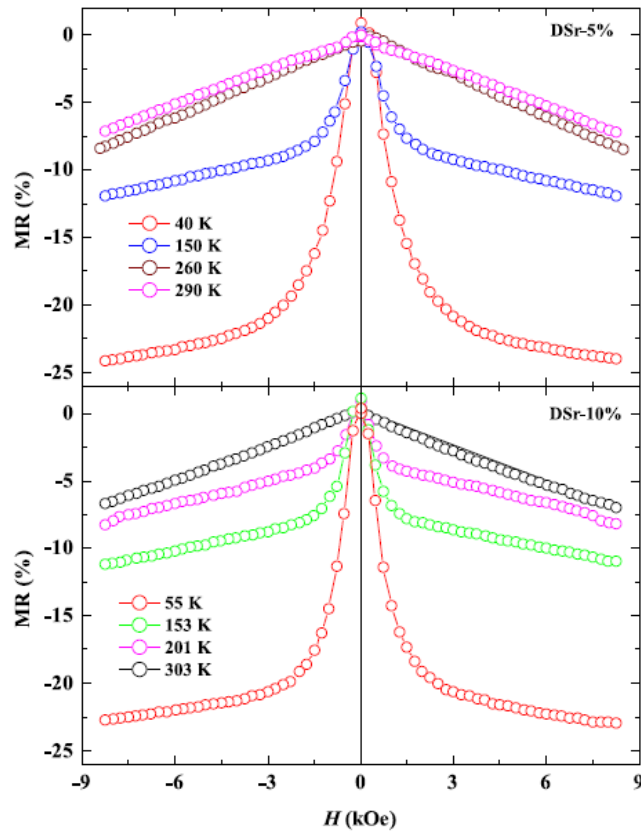

Fig. 6. MR as a function of field (H) at selective temperatures for DSr–5% and DSr–10%.

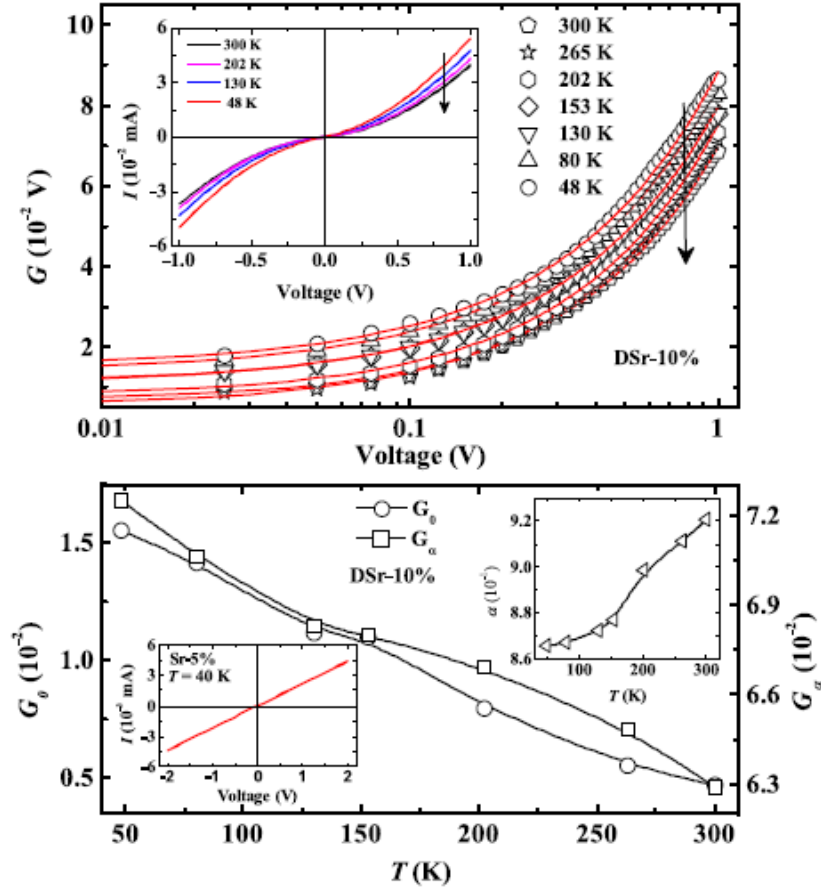Fig. 7. Top panel: GV–V curves at selective temperatures. The solid lines exhibit the fits using Eq. (1). Inset exhibits I–V curves at selective temperatures. Bottom panel: The temperature dependence of the coefficients G0 and Gα are obtained from Eq. (1). Upper inset shows the temperature dependence of α. Lower inset shows I–V curve for Sr − 5%.

The isothermal magnetization of the compounds is measured as a function of field at 5 and 300 K and is shown in Fig. 5. All the data were recorded after cooling the sample from 400 K and then stabilized at 5 and 300 K. Except for the sample Sr − 5%, at 5 K, magnetization initially increases rapidly with H and saturates at ≈1.0 T, indicating the characteristic features of soft ferromagnet for all La-deficient samples. However, the magnetic saturation is not observed for Sr − 5% with the applied magnetic field up to the 5 T. The inset of the top panel of Fig. 5 shows that the rate of increase of M with H decreases in the high magnetic field region (2 T≤H≤10 T) and no saturation is observed even at 10 T. The value of saturation magnetic moments (μ_{sat}) was calculated from the magnetic moment extrapolated at 1/H=0 in the plot of M vs 1/H at 5 K μ_{sat} of Sr − 5% shows a large deviation from μ_{sat}^{th} explaining the presence of antiferromagnetic interactions accompanying with cluster/spin glass (SG) behavior [24,25]. μ_{sat} at 5 K and 5 T are listed in Table 2. The value of μ_{sat} suggests the oxygen stoichiometry ≈3 for DSr − 0%, and is consistent with reported result [8]. The relatively small value of μ_{sat} (also μ_{sat}^{th}) in DSr–10% compared to that of DSr–0% is a measure of Mn^{4+} doping in this compound however for DSr–5%, the value of μ_{sat} comes out much higher than that of corresponding μ_{sat}^{th} . This difference suggests that the system with DSr −5% is having a probable presence of Mn^{2+} (in high spin state) along with Mn^{4+} however our X-ray diffraction did not show the existence of any multi-phase structure for this compound. The high value of

μ_{sat} for DSr −5% is therefore anomalous and needs to be probed further. The nonlinearity of M–H curve at 300 K (the lower panel of Fig. 5) for DSr−10%, DSr − 5%, DSr − 0% might be ascribed to the presence of short range FM clusters at 300 K satisfying Curie–Weiss behavior. At 300 K for Sr−5%, i.e., above T_C, the quasi-linear M(H) curve is the indication of paramagnetic nature of sample at that temperature.

We observed the nature of low-field MR at selected temperatures by varying the magnetic field up to ±8.5 kOe for DSr − 5% and DSr −10%. The plots of MR are shown in Fig. 6, exhibiting different characteristic features at different temperatures for DSr − 5% and DSr −10%. The nature of MR-H curves at 40 and 150 K are similar, while at 40 K, we observed 24% MR value at 8.5 kOe field for DSr − 5% (top panel of Fig. 6). In the bottom panel of Fig. 6 shows the similar nature of MR-H curves at 55, 153 and 201 K for DSr − 10% and the maximum value of MR estimates 23% at 55 K and 8.5 kOe of applied field. The linear variation of MR with H is shown around the T_C at 290 and 303 K for DSr − 5% and DSr − 10%, respectively. MR increases monotonically with decreasing temperature indicating the feature of spin tunneling through the grain boundary (GB) region [33]. Similar lowfield MR behavior was also observed for DSr − 0% and Sr − 5% as reported earlier [24,33].

In order to understand the electronic transport mechanism at low temperature that involves tunneling across the GB, the current-voltage (I–V) curves were measured at selective temperatures in zero magnetic field. The nonlinear I–V characteristic of DSr −0% was reported in our early study [33] and interpreted in terms of inelastic tunneling via localized states. The I–V curves of DSr − 5% are qualitative similar to the curves which were taken for DSr − 10%, although they differ in quantitative details. However, to avoid duplicity, the data for DSr − 5% is not given. In contrast, the linear I–V characteristic of Sr − 5% has been examined where ohmic conductivity is observed up to±2 V as shown in lower inset of bottom pannel of Fig. 7. The signature of nonlinear curves at selective temperatures for DSr − 10% in the range 48–300 K are shown in the inset of top panel of Fig. 7. The nonlinearity of I–V curves at different temperatures are depicted in top panel of Fig. 7 through the dynamic conductance, G(V, T) for T≤T_C where G(V,T) is defined as dI/dV which is obtained by the numerical differentiation of the I–V curves. The weight of nonlinear transport is investigated by fitting the voltage dependent conductance at different temperatures to the phenomenological relation [34].

$$G(V,\ T) = G_0\,(T) + G_\alpha\,(T)|V|^\alpha \qquad (1)$$

where the nonlinearity is interpreted through the conductance exponent, α and the weight factor, G_α. G_0 denotes the conductance in the zero voltage limit. Eq. (1) has been used extensively to interpret the nonlinear transport in manganites [34–37]. We fit the observed G(V,T) – V data for DSr–10% to Eq. (1) over the whole voltage range and at all temperatures (48–300 K). With this, bottom panel of Fig. 7 shows the temperature dependence of the three parameters obtained from the fits. G_0 and G_α decrease monotonically with increasing temperature. The obtained fitted parameters, G_α and G_0 varied from 0.07251 to 0.06291 and 0.01553 to 0.00471, respectively. However, α increases monotonically from 0.86553 at 48 K to 0.9206 at 300 K which is shown in the upper inset of bottom panel of Fig. 7. The variation of α(T) is more steeper at the high temperature region (153 K≤T≤300 K). In the case of direct elastic tunneling through the GB barrier, the exponent α equals to 2 at low voltages described by the

quantum tunneling theory of Simmons [38]. If the transport is dominated by the inelastic tunneling via localized states at GB, Glazman and Matveev [39] predicted that α is nonquadratic. Recently, from the investigation in bulk $La_{0.9}MnO_3$ a value of α=1.25–1.5 suggested that inelastic tunneling via localized states is dominant in transport mechanism at low temperatures [33]. The dependence of G_α and α with temperature indicates that the nonlinear I–V behavior in same biasing voltage increases with increase of temperature in the entire temperature range. The temperature and field dependence of α, G_α and G_0 suggest that the inelastic tunneling via localized states is dominant in the transport mechanism.

In summary, The low temperature metallic behavior with a characteristic feature of metal to semiconducting transition accompanying with a typical feature of FM character are observed for all compounds. The compound with Sr − 5% shows different characteristic features such as two FM ordering temperatures at T_{C1} and T_{C2}, absence of sharp peak at Tp in ρ(T), and linear ohmic I–V behavior below T_C. Increasing Mn^{4+} content with Sr content as well as La deficiency commits the hole-rich FM and metallic phases. The distinct behavior of low field MR below T_C is suggested due to the tunneling of electrical transport across the GB region. The analysis of the nonlinear current-voltage curves for La deficient samples further indicates that the inelastic tunneling via localized states of the GB region is dominant.

Journal Paper published in this project:

1. De-stabilization of charge order state through in-homogeneity in random ionic distribution in the particles of polycrystalline $Eu_{0.2}La_{0.3}Sr_{0.2}Ca_{0.3}MnO_3$ sample, Bulletin of Materials Science, K De, P Dhak, S De, P Dutta, K Dey, S Mukherjee, S Chatterjee and S Das, 43, 112 (2020)

2. Magnetic and electrical transport of the cation-deficient LaMnO3: Common origin of both Sr-doping and self-doping effects, S. Das, P. Roychoudhury, S. De, S Chatterjee, and K. De, Physica B: Condensed Matter 544, 17-22 (2018)

3. Low-temperature localization in the transport properties of self doped $La_{0.9}Mn_{0.98}Zn_{0.02}O_3$, K. De and S. Das, Bulletin of Materials Science, 39, 293-298 (2016)

Conference Paper presented:

Enhanced Ferromagnetic Behaviour and Glassy State in Low Doped $La_{0.95}Sr_{0.05}MnO_{3+\delta}$, S. Das, K. De, 25th National Symposium on Cryogenics NSC-25, Hyderabad, 8-10 December, 2014

References:

[1] Y. Tokura, N. Nagaosa, Science 288 (2000) 462.
[2] E. Dagotto, T. Hotta, A. Moreo, Phys. Rep. 344 (2001) 1.
[3] C. Zener, Phys. Rev. 82 (1951) 403.
[4] A. Urushibara, Y. Moritomo, T. Arima, A. Asamitsu, G. Kido, Y. Tokura, Phys. Rev. B 51 (1995) 14103.
[5] S. Nair, A. Banerjee, A.V. Narlikar, D. Prabhakaran, A.T. Boothroyd, Phys. Rev. B 68 (2003) 132404.
[6] Y. Endoh, K. Hirota, S. Ishihara, S. Okamoto, Y. Murakami, A. Nishizawa, T. Fukuda, H. Kimura, H. Nojiri, K. Keneko, S. Maekawa, Phys. Rev. Lett. 82 (1999) 4348.
[7] S. de Brion, F. de Ciorcas, G. Chouteau, P. Lejay, P. Radaelli, C. Chaillout, Phys. Rev. B 59 (1999) 1304.
[8] I.O. Troyanchuk, V.A. Khomchenko, M. Tovar, H. Szymczak, K. Barner, Phys. Rev. B 69 (2004) 054432.

[9] K. De, S. Majumdar, S. Giri, J. Phys. Condens. Matter 19 (2007) 096205.

[10] K. De, S. Majumdar, S. Giri, J. Phys. D: Appl. Phys. 40 (2007) 5810.

[11] M. Patra, K. De, S. Majumdar, S. Giri, Appl. Phys. Lett. 94 (2009) 092506.

[12] I. Solovyev, N. Hamada, K. Terakura, Phys. Rev. Lett. 76 (1996) 4825.

[13] S. Wang, S. Du, W. Tang, S. Hoang, X. Lu, W. Xiao, B. Zhang, J. Weng, E. Schneer, Y. Guo, J. Ding, Z. Zhang, P. Gao, ChemCatChem (2018), 1002/cctc.201702048.

[14] M. Pavone, A.B. Muñoz-García, A.M. Ritzmann, E.A. Carter, J. Phys. Chem. C 118 (25) (2014) 13346.

[15] C. Ritter, M.R. Ibarra, J.M. De Teresa, P.A. Algarabel, C. Marquina, J. Blasko, J. Garcia, S. Oseroff, S.-W. Cheong, Phys. Rev. B 56 (1997) 8902.

[16] J. Töpfer, J.B. Goodenough, J. Solid State Chem. 130 (1997) 117.

[17] F. Prado, R.D. Sánchez, A. Caneiro, M.T. Causa, M. Tovar, J. Solid State Chem. 146 (1999) 418.

[18] M. Muroi, R. Street, Aust. J. Phys. 52 (1999) 205.

[19] K. De, R. Ray, R.N. Panda, S. Giri, H. Nakamura, T. Kohara, J. Magn. Magn Mater. 288 (2005) 339.

[20] K. De, A. Roy, C.J.R. Silva, M.J.M. Gomes, Solid State Commun. 150 (2010) 1187.

[21] J.-S. Kang, Y.J. Kim, B.W. Lee, C.G. Olson, B.I. Min, J. Phys. Condens. Matter 13 (2001) 3779.

[22] M.S. Kim, J.B. Yang, Q. Cai, X.D. Zhou, W.J. James, W.B. Yelon, P.E. Parris, D. Buddhikot, S.K. Malik, Phys. Rev. B 71 (2005) 014433.

[23] K.R. Mavani, P.L. Paulose, Phys. Rev. B 72 (2005) 104421.

[24] K. De, S. Das, A. Roy, P. Dhak, M. Willinger, J.S. Amaral, V.S. Amaral, S. Giri, S. Majumder, C.J.R. Silva, M.J.M. Gomes, P.K. Mahapatra, J. Appl. Phys. 112 (2012) 103907.

[25] S. Das, J.S. Amaral, K. De, M. Willinger, J.N. Goncalves, A. Roy, P. Dhak, S. Giri, S. Majumder, C.J.R. Silva, M.J.M. Gomes, P.K. Mahapatra, V.S. Amaral, Appl. Phys. Lett. 102 (2013) 112408.

[26] K. De, S. Majumdar, S. Giri, J. Magn. Magn Mater. 322 (2010) 337.

[27] J.M.D. Coey, M. Viret, S. von Molnar, Adv. Phys. 48 (1999) 167.

[28] E. Dagotto, T. Hotta, A. Moreo, Phys. Rep. 344 (2001) 1.

[29] D.C. Kundaliya, R. Vij, R.G. Kulkarni, A.A. Tulapurkar, R. Pinto, S.K. Malik, W.B. Yelon, J. Magn. Magn Mater. 264 (2003) 62.

[30] K. De, M. Patra, S. Majumdar, S. Giri, J. Phys. D: Appl. Phys. 40 (2007) 7614.

[31] F. Millange, S. de Brion, G. Chouteau, Phys. Rev. B 62 (2000) 5619.

[32] A. Biswas, I. Das, J. Appl. Phys. 102 (2007) 064303.

[33] M. Patra, A. Roy, K. De, S. Majumdar, S. Giri, Appl. Phys. Lett. 94 (2009) 212107.

[34] M. Ziese, Phys. Rev. B 60 (1999) R738.

[35] M. Paranjape, J. Mitra, A.K. Raychaudhuri, N.K. Todd, N.D. Mathur, M.G. Blamire, Phys. Rev. B 68 (2003) 144409.

[36] N. Khare, U.P. Moharil, A.K. Gupta, A.K. Raychaudhuri, S.P. Pai, R. Pinto, Appl. Phys. Lett. 81 (325) (2002).

[37] R. Shao, J. Vavro, D.A. Bonnell, Appl. Phys. Lett. 85 (2004) 561.

[38] J.G. Simmons, J. Appl. Phys. 34 (1963) 1793.

[39] L.I. Glazman, K.A. Matveev, Sov. Phys. JETP 67 (1988) 1276.

CrossMark

Low-temperature localization in the transport properties of self-doped $La_{0.9}Mn_{0.98}Zn_{0.02}O_3$

K DE[1] and S DAS[2],*

[1]Neotia Institute of Technology, Management and Science, Jhinga 743 368, India
[2]Department of Electronics and Communication Engineering, Guru Ghasidas Central University,
Bilaspur (C.G.) 495 009, India

Abstract. Low-temperature transport properties are investigated in the self-doped compound, $La_{0.9}Mn_{0.98}Zn_{0.02}O_3$. The analysis of the low-temperature resistivity is performed considering various scattering mechanisms. The parameters involved with different scattering processes such as electron–electron, Kondo, electron–phonon and electron–magnon are found to be strongly influenced by the applied magnetic field. The results suggest that interplay between electron–electron and Kondo-like scatterings lead to the localization in the temperature dependence of resistivity at low temperature.

Keywords. Transport properties; scattering mechanisms; low temperature localization.

1. Introduction

The investigation on mixed-valent manganites with perovskite structure is on run for the last two decades. Specially, the studies on the hole doped manganites, $La_{1−\delta}A_{\delta}MnO_3$ (A = divalent atom) still demands special attention because of the intriguing magnetic and transport properties [1–5]. In recent times, the self-doped manganites with composition $La_{1−\delta}MnO_\varrho$ also display analogous features in the magnetic, transport and structural properties depending on ϙ and δ [6–15]. Mn^{4+} appears in these compounds due to the La deficiency, leading to the spectacular changes in the physical properties.

In recent times, the electronic transport in few manganites displays localization effect in the metallic region at low temperature, suggesting different opinions [16–23]. The low-temperature localization in resistivity was suggested due to the grain boundary effect in $La_{0.5}Pb_{0.5}MnO_3$ [16]. The electron–electron (e–e) scattering ascribed to the enhanced Coulomb interaction was interpreted in $La_{0.8}Sr_{0.2}MnO_3$ and thin film of $La_{0.7}Ca_{0.3}MnO_3$ [17,18]. The coexistence of Kondo-like behaviour and e–e scattering has been proposed in the polycrystalline hole doped manganites, $La_{2/3}Ca_{1/3}MnO_3$ and Y-doped $(La_{1−\delta}Y_{\delta})_{2/3}Ca_{1/3}MnO_3$ [20,21]. The increase of localization effect as a result of minor Co and Fe substitutions has also been investigated in $La_{0.87}Mn_{0.98}M_{0.02}O_3$ (M = Fe and Co) where minor magnetic impurity or spin-glass-like phase appeared due to the substitution resulted in the dominant localization effect [22,23]. In contrast to the substitution by magnetic impurity such as Fe and Co, the substitution of nonmagnetic Zn

also decreases the conductivity and lowering of Curie temperature in $La_{0.91}Mn_{0.95}Zn_{0.05}O_3$ [24]. Signature of glassy magnetic behaviour and decrease of conductivity ascribed to the disorder created by the Zn substitution was observed in $LaMn_{1−x}Zn_xO_3$ [25]. The minor Zn substitution in hole doped, $La(Ca)MnO_3$ modifies the grain boundary, resulting in the decrease of conductivity [26–28].

In this article, the low-temperature localization effect due to the minor Zn substitution in $La_{0.9}Mn_{0.98}Zn_{0.02}O_3$ is investigated. At low temperature the localization effect is confirmed due to the interplay between e–e and Kondo scatterings in accordance with the reported phenomenological models.

2. Experimental

The polycrystalline compound with composition $La_{0.9}Mn_{0.98}Zn_{0.02}O_3$ was prepared by the chemical route as described in our earlier literature [29]. The final annealing was performed at 1200°C for 12 h in air followed by furnace cooling down to room temperature. In order to avoid ambiguity ascribed to the oxygen non-stoichiometry, sample was again annealed in atmospheric pressure of oxygen for 6 h at 1000°C. The single phase of the sample was confirmed by the powder X-ray diffraction (XRD) (Seiferd XRD 3000P) using CuK_α radiation. All the diffraction peaks could be indexed in the rhombohedral structure $(R\bar{3}c)$ with lattice parameters a = 5.47(2) Å and α = 60.59°. Scanning electron microscopy (SEM) image in figure 1 shows the size and morphology of the grains in the sample. The particles exist as big grains with not well-defined edges. The inhomogeneity of the grain size with average diameter ≈ 90 nm was noticed
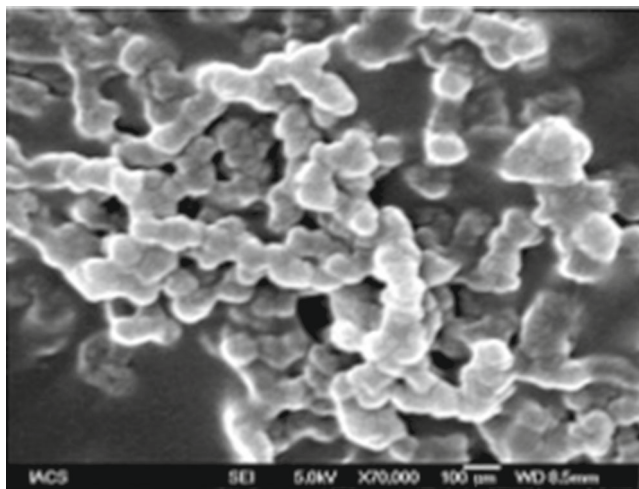
*Author for correspondence (soma.iitkharagpur@gmail.com)

Figure 1. SEM image for $La_{0.9}Mn_{0.98}Zn_{0.02}O_3$.

Figure 2. Temperature dependence resistivity (ρ) in zero field for compounds $La_{0.9}Mn_{0.98}Zn_{0.02}O_3$ and $La_{0.9}MnO_3$.

Figure 3. Temperature dependence resistivity (ρ) under ZFC condition with different applied fields, the solid lines indicate the fitted results by using equation (3).

in the SEM observation. The resistivity (ρ) was measured using the standard four-probe technique where application of the magnetic field and temperature variation were carried out by an electromagnet (Polytronic Corp., India) and a cryogen-free cryostat operating down to 10 K (Janis Research Inc., USA), respectively. Magneto-resistance (MR) is defined as $\left[\{\rho(H) - \rho(H = 0)\} / \rho(H = 0) \right]$ where $\rho(H)$ is the resistivity measured in field (H). All the thermal variation during resistivity measurement was carried out at a fixed rate of 2 K min^{-1}. The magnetization (M) was measured using a commercial superconducting quantum interference device (SQUID) magnetometer (MPMS, XL). In case of zero-field cooled (ZFC) mode the sample was cooled down to the desired temperature at zero magnetic field while for the field-cooled (FC) mode the sample was cooled in a static magnetic field.

3. Results and discussions

Temperature variation of resistivity ρ measured in zero-field and 2 kOe field is shown in figure 2 for $La_{0.9}Mn_{0.98}Zn_{0.02}O_3$. A sharp peak in resistivity ρ is observed at 235 K (T_P) which is accompanied by a broad maximum around $\sim$175 K (T_m). The features in the temperature dependence of resistivity ρ are in accordance with the parent compound, $La_{0.9}MnO_3$ where T_P and T_m are shifted towards the low temperature in the present observation. The result is also consistent with those reported in $La_{0.9}Mn_{1-x}Fe_xO_3$ ($0 \leq x \leq 0.05$) [22] and $La_{0.9}Mn_{0.98}M_{0.02}O_3$ ($M = O$, Fe and Co) [23]. It was noted that the considerable increase of ρ involved with the minimal Zn substitution in the entire temperature range compared to the parent compound. This is in accordance with the minor Zn substitution in $LaMnO_3$ as well as hole doped, $La(Ca)MnO_3$ where disorder introduced by the Zn substitution, partial disruption of double-exchange interaction, modification of the grain boundary effect have been proposed to interpret the results [25–27].
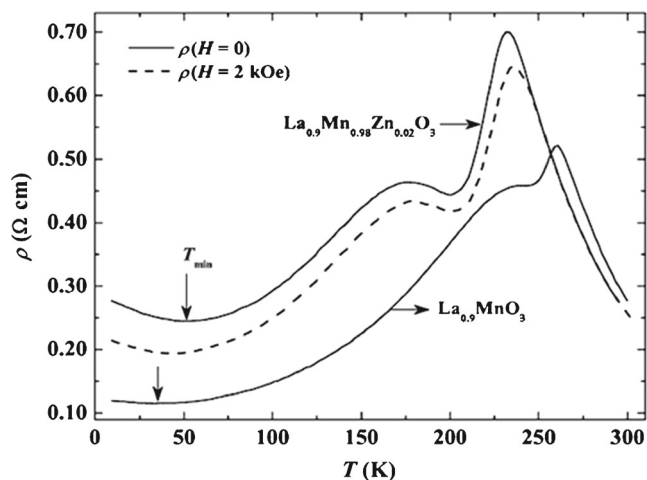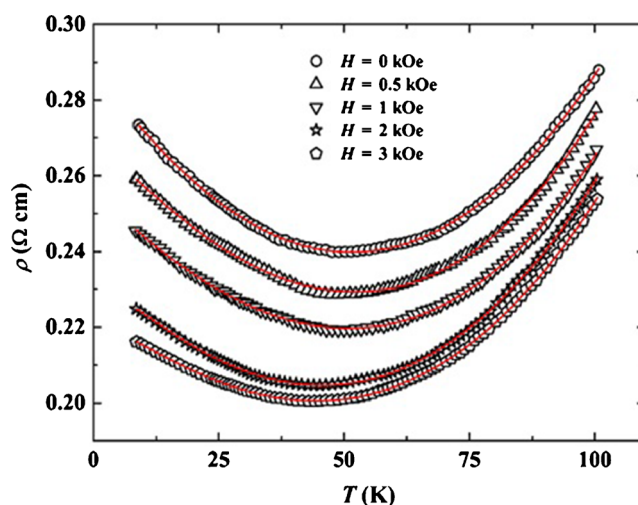
Temperature dependence of ρ by varying field, H ranging from 0 to 3.0 kOe is shown in figure 3 below 100 K. It has been noted that resistivity minimum appeared at T_{min} is shifted towards high temperature compared to the parent compound [23]. Furthermore, T_{min} shows the strong field dependence where T_{min} is shifted towards low temperature with the increase field which is shown in the inset of figure 4. In figure 4 the resistivity upturn, ρ_{10K} defined as $\{\rho_{10K} - \rho(T_{min})\} / \rho(T_{min})$ (%) is plotted as a function of H where ρ_{10K} and $\rho(T_{min})$ are the resistivities at 10 K and minimum in the temperature dependence of ρ, respectively. The plot clearly demonstrates that low-T resistivity is strongly influenced by the magnetic field. Therefore, it can be suggested that the spin-dependent scattering must be associated with the resistivity minima of this sample which is gradually suppressed by external magnetic field.
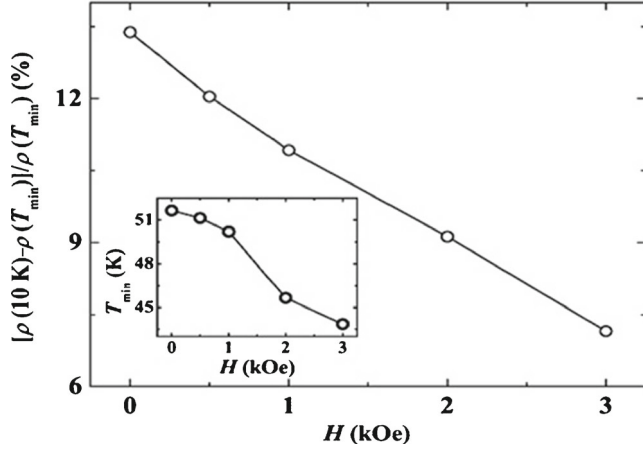
Figure 4. $\Delta\rho_{10K} = (\rho_{10K} - \rho(T_{min}))/\rho(T_{min})$ (%) as a function of the applied field. The inset shows the dependence of T_{min} on the applied field, H.
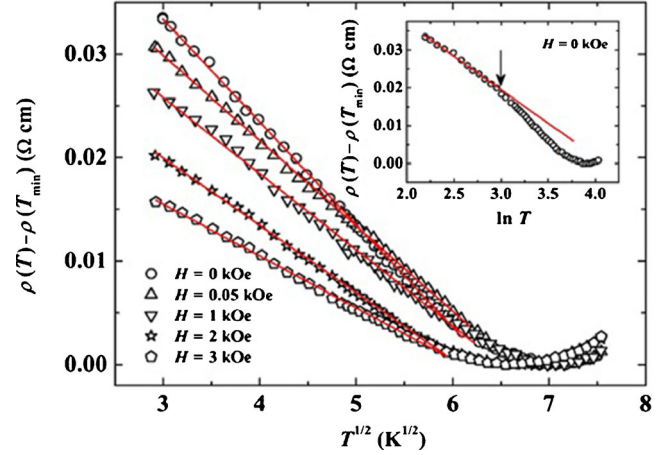

Figure 5. $T^{1/2}$ dependence of resistivity subtracted the minimum value defined as $\rho(T) - \rho(T_{min})$ under different applied fields ($H \leq$ 3 kOe). The solid lines are the fitting results. The inset shows the dependence of $\ln T$ with $\rho(T) - \rho(T_{min})$, where solid lines are indicated the linear fits.

In order to elucidate the origin of low-T upturn different phenomenological models have been proposed considering spin-dependent Kondo-like scattering, e–e interaction, weak localization, inter-granular tunnelling of polarized charge carriers, etc [16–21]. The e–e scattering due to Coulomb interaction between the charge carriers has been proposed in references [30–32]. Note that interpretation using e–e may be adopted in the analysis when the magnitude of low-temperature resistivity is higher than Motts maximum limit of metallic resistivity with $\rho \approx 10$ mΩ cm [30,31], which for the present sample is well satisfied. In order to test the possible e–e interaction, $T^{1/2}$ dependence of $\rho(T) - \rho_{min}$ at different H is plotted in figure 5 for $T \leq T_{min}$. The figure shows that the plots fit satisfactory over a wide temperature range below T_{min} at different fields. We also tried to fit all the curves by taking into account the Kondo scattering term $\ln(T)$ which has been used to fit the low-T resistivity in few manganites [18,20,21]. The inset of figure 5 shows the $\ln(T)$ dependence of resistivity in zero field. The plot indicates that it fits satisfactorily in a limited low-temperature region which departs at much lower temperature than T_{min} indicated by the arrows in the figure. In addition to the elastic e–e scattering and Kondo-like scattering, the resistivity in the metallic region is ascribed to the various inelastic contributions such as electron–phonon and electron–magnon scattering processes. At low temperature e–e and Kondo scatterings dominate while the inelastic term dominates at high temperature. Therefore, the resistivity may be defined by adding both the elastic and inelastic scattering terms as

$$\rho = \rho_{elastic} + \rho_{inelastic}. \tag{1}$$

Considering elastic e–e scattering, $\rho_{elastic}$ is given by $\rho_{elastic} = 1/\left[\sigma(0) + BT^{1/2}\right]$ where $\sigma(0)$ is the residual conductivity and B the constant [30,31]. The inelastic scattering term is given by a power law, $\rho_{inelastic} = AT^n$. This single power law adequately describes all the temperature-dependent inelastic

scattering processes at high temperature. Thus, equation (1) is redefined as

$$\rho(T) = \frac{1}{\sigma(0) + BT^{1/2}} + AT^n. \tag{2}$$

The interplay between these two temperature-dependent terms in equation (2) leads to the resistivity minimum in the temperature dependence. At low field the grain boundary effect is also typically observed in the magneto-resistance for granular manganites having ferromagnetic ground state [15,33]. Therefore, as discussed before, in addition to the elastic e–e scattering, a Kondo scattering term $\ln(T)$ has been introduced for interpreting the low-T upturn [20,21] and it has been noted that the degree of fitting (χ^2) is improved further by one order of magnitude after considering this additional $\ln(T)$ term for the analysis of the experimental data. Thus, the following phenomenological relation [20,21], where all the scattering terms are separated:

$$\rho(T) = \rho_0 + \rho_e T^{1/2} - \rho_s \ln T + \rho_p T^n \tag{3}$$

is used to fit the $\rho(T)$ data for all H and is shown by the solid lines in figure 6. The low values of $\chi^2 (\sim 10^{-7})$ give satisfactory fit with the experimental data. The strong magnetic field dependence is noticed in all the fitted parameters. Inelastic term involved with the electron–phonon and electron–magnon scattering is found to be several orders of magnitude smaller than the other contributions. Inelastic scattering exponent (n) is found in between 2.39 and 2.75 (table 1) which is close to that observed in La$_{1-\delta}$Ca$_\delta$MnO$_3$ by Schiffer *et al* [34] with $n = 25$. Table 1 shows that the values of ρ_0, ρ_e and ρ_s decrease monotonically with applied magnetic analogous to that observed in La$_{09}$Mn$_{098}$M$_{002}$O$_3$ (M = O, Fe and Co), La$_{2/3}$Ca$_{1/3}$MnO$_3$ and Y-doped (La$_{1-\delta}$Y$_\delta$)$_{2/3}$Ca$_{1/3}$MnO$_3$ [20,21,23]. The decrease of residual resistivity ρ_0 with the increase in H is different from the usual conductor where
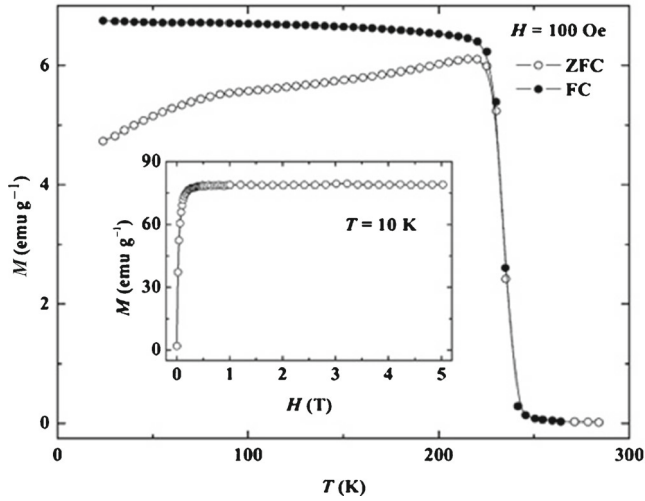
Figure 6. Temperature dependence of ZFC (open symbols) and FC (solid symbols) magnetizations in an applied field of 100 Oe. Inset shows the magnetization as a function of applied field at 10 K.

Table 1. Parameters are obtained from the fits of $\rho - T$ curves in figure 3 to equation (3).

H (kOe)	ρ_0	ρ_e	ρ_s	ρ_p (10^{-6})	n	χ^2 (10^{-7})
0	0.297	0.020	0.018	1.99	2.39	1.10
0.5	0.276	0.018	0.016	0.42	2.69	3.60
1.0	0.263	0.014	0.015	0.28	2.75	1.50
2.0	0.238	0.012	0.013	1.43	2.45	0.77
3.0	0.226	0.012	0.012	0.47	2.65	0.38

ρ_0 generally is independent of T and H. In case of manganites, ρ_0 may be related to intrinsic properties of system and reflects CMR effect and disorder characteristics of the system. From table 1, ρ_p does not show monotonic change with H and may be interpreted to be field insensitive and is smaller in few orders of magnitudes than the other effects at low temperatures. Compared to ρ_p (the inelastic scattering), the values of ρ_e and ρ_s are much higher, both are positive and comparable to each other at all fields. Both are monotonically decreasing with the increase in field. This explains the decrease of resistivity with field at low temperature due to suppression of spin-dependent scattering resulting in $\Delta\rho_{10K}$ and shifting of T_{min} at lower temperature. In case of $La_{2/3}Ca_{1/3}MnO_3$ the Kondo scattering was found to be negligible for $H \geq 10$ kOe [21]. Herein, Kondo scattering had to be taken into account even at 3.0 kOe. A good agreement between the experimental data and fitting results provides the possibility to understand resistivity minimum at low temperatures using the theory of both e–e interaction and Kondo-like scattering.

In order to understand the interesting change of the spin scattering strength, dc magnetization measurements in the field cooling (FC) and zero field cooling (ZFC) modes were performed. Figure 6 shows the temperature dependence of ZFC magnetization M_{ZFC} and FC magnetization M_{FC} at low

field, $H = 0.01$ T. A sharp PM to FM transition is observed at T_C, as determined from the deep in the plot of temperature derivation of FC magnetization (dM_{FC}/dT) with T. The value of T_C was estimated to be 235 K which coincides the value of T_P in $\rho(T)$. Large thermo-magnetic irreversibility is observed below T_C. The degree of separation of the $M–T$ curves reflects the degree of the strength of the spin disorder. It is well known that this separating phenomenon of MT curve is a possible AFM or the spin-glass (SG) characteristic.

In relation with this observation, the nature of low field MR at selected temperatures has also been studied by varying the magnetic field up to 5.0 kOe. The plots of MR are shown in the inset of figure 7, exhibiting different characteristic features at different temperatures. The nature of MR–H curves at 200, 175 and 113 K are similar. In contrast, the MR at 235 K (T_C) is linearly depended on field and having the value of MR is $\approx 19\%$ at 5.0 kOe. The MR–H curve at 50 K in figure 7 shows a sharp decrease initially up to ≈ 15 kOe and then it decreases further almost linearly from 3 kOe to higher field. Initial rapid decrease in MR exhibits the typical feature of grain boundary-assisted tunnelling magnetoresistance while the high-field linear component manifests the intrinsic component attributed to the double-exchange mechanism [15,33]. Here, the contribution of Kondo term decreases monotonically with the increase in field and it is still observed until 3.0 kOe. This is reasonable because the contribution to the magneto-resistance from grain boundary effect still exists in the polycrystalline compound as seen in figure 7. If we compare both $M–H$ curve at 10 K and MR curve at 50 K as seen in figure 8, we observe that $M–H$ curve has typical ferromagnetic characteristics where M increases sharply with the increase in field and started to get saturation near 3.0 kOe. MR also shows similar changes correspondingly, i.e., it decreases sharply with the increase in field and then almost linearly at around 3.0 kOe. This correlation between electrical transport and magnetic properties at lower
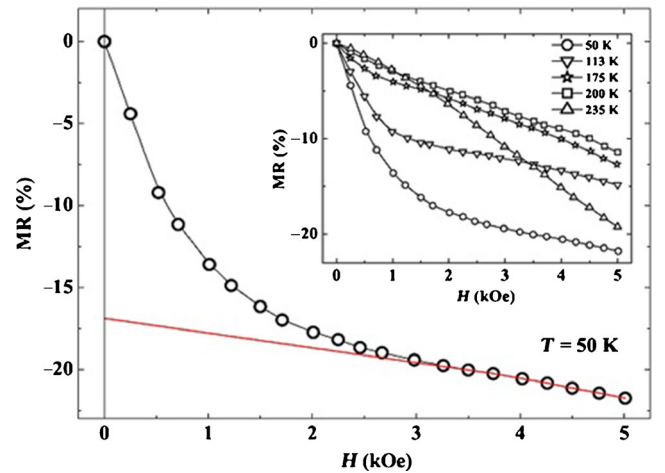

Figure 7. Magnetoresistance (MR) curve is plotted with field (H) at 50 K. High field range satisfying linear dependence is indicated by the straight line. Inset shows the MR at different temperatures.
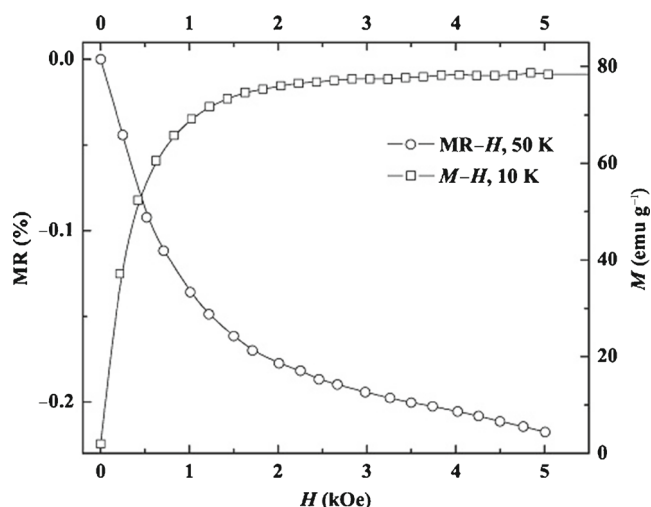
Figure 8. Simultaneous dependence of magnetoresistance (MR) and magnetization (M) on the applied magnetic field at 50 and 10 K, respectively.

field reflects grain boundary contribution in the system at low temperature.

Finally, as a result of Zn substitution a minor spin-glass-like state was also reported in LaMn$_{1-x}$Zn$_x$O$_3$ [25]. The increase of low-temperature localization in the transport property was attributed to the minor spin-glass-like state in La$_{09}$Mn$_{098}$Fe$_{002}$O$_3$ [22,23] and Y-doped (La$_{1-\delta}$Y$_\delta$)$_{2/3}$ Ca$_{1/3}$MnO$_3$ [20]. Here, dominant grain boundary effect is considered to be involved with the appearance of minor spin-glass-like state due to the Zn substitution which has an addition localization effect associated with the electron–electron scattering in the transport properties at low temperature.

4. Conclusions

In summary, low-T transport properties are investigated in the self-doped compound, La$_{09}$Mn$_{098}$Zn$_{002}$O$_3$. The analysis of the low-T resistivity using phenomenological model indicates the interplay among contributions from electron–electron, Kondo, electron–phonon and electron–magnon scatterings leading to the minimum in the temperature dependence of resistivity. The analysed parameters involved with different scattering processes strongly depend on the applied low magnetic field. The localization effect at low temperature is suggested due to the coexistence of electron–electron and Kondo-like scatterings in the transport properties. The correlation between low-temperature M curve and MR curve supports the grain boundary contribution and grain boundary-assisted tunnelling in the system.

Acknowledgements

References

[1] Dagotta E, Hotta T and Moreo A 2001 *Phys. Rep.* **344** 1

[2] Salamon M B and Jaime M 2001 *Rev. Mod. Phys.* **73** 583

[3] Ramirez A P 1997 *J. Phys.: Condens. Matter* **9** 8171

[4] Imada M, Fujimori A and Tokura Y 1998 *Rev. Mod. Phys.* **70** 039

[5] Rao C N R and Raveau B 1998 *Colossal magnetoresistance, charge ordering and related properties of manganese oxides* (Singapore: World Scientific)

[6] Arulraj A, Mahesh R, Subbanna G N, Mahendiran R, Raychaudhuri A K and Rao C N R 1996 *J. Solid State Chem.* **127** 87

[7] de Brion S, Ciorcas F, Chaillout G, Lejay P, Radaelli P and Chaillout C 1999 *Phys. Rev. B* **59** 1304

[8] Troyanchuk I O, Khomchenko V A, Chobot A N and Szymczak H 2004 *Phys. Rev. B* **69** 054432

[9] Troyanchuk I O, Khomchenko V A, Chobot A N and Szymczak H 2003 *J. Phys.: Condens. Matter* **15** 6005

[10] Joy P A, Raj Sankar C and Date S K 2002 *J. Phys.: Condens. Matter* **14** L663

[11] Muroi M, Street R, Cochrane J W and Russell G J 2000 *Phys. Rev. B* **62** R9268

[12] De K, Majumdar S and Giri S 2007 *J. Phys.: Condens. Matter* **19** 096205

[13] De K, Majumdar S and Giri S 2007 *J. Phys.: Condens. Matter* **19** 096205

[14] Patra M, De K, Majumdar S and Giri S 2009 *Appl. Phys. Lett.* **94** 092506

[15] Patra M, Roy A, De K, Majumdar S and Giri S 2009 *Appl. Phys. Lett.* **94** 212107

[16] Rosenberg E, Auslender M, Felner I and Gorodetsky G 2000 *J. Appl. Phys.* **88** 2578

[17] Auslender M, Karkin A E, Rosenberg E and Gorodetsky G 2001 *J. Appl. Phys.* **89** 6639

[18] Kumar D, Sankar J, Narayan J, Singh R K and Majumdar A K 2002 *Phys. Rev. B* **65** 094407

[19] Rana D S, Markna J H, Parmar R N, Kuberkar D G, Raychaudhuri P, John J and Malik S K 2005 *Phys. Rev. B* **71** 212404

[20] Zhang J, Xu Y, Cao S, Cao G, Zhang Y and Jing C 2005 *Phys. Rev. B* **72** 054410

[21] Xu Y, Zhang J, Cao G and Cao S 2006 *Phys. Rev. B* **73** 224410

[22] De K, Majumdar S and Giri S 2007 *J. Phys. D: Appl. Phys.* **40** 5810

[23] De K, Majumdar S and Giri S 2010 *J. Magn. Magn. Mater.* **322** 337

[24] Markovich V, Rozenberg E, Gorodetsky G, Mogilyansky D, Revzin B and Pelleg J 2001 *J. Appl. Phys.* **90** 2347

[25] Alvarez-Serrano I, Pico C and Veiga M L 2004 *Solid State Sci.* **6** 1321

[26] Ghosh K, Ogale S B, Ramesh R, Greene R L, Venkatesan T, Gapchup K M, Bathe R and Patil S I 1999 *Phys. Rev. B* **59** 533

[27] Seetha Lakshmi L, Dörr K, Nenkov K, Sastry V S and Müller K-H 2007 *J. Phys.: Condens. Matter* **19** 236207

[28] El-Fadli Z, Redouane Metni M, Sapina F, Martinez E, Folgado J V and Beltrán A 2002 *Chem. Mater.* **14** 688

[29] De K, Ray R, Panda R N, Giri S, Nakamura H and Kohara T 2005 *J. Magn. Magn. Mater.* **288** 339

[30] Lee P A and Ramakrishnan T V 1985 *Rev. Mod. Phys.* **57** 287

[31] Altshuler B L and Aronov A G 1985 In: Efros A L and Pollak M eds *Electron–electron interactions in disordered systems* (Amsterdam: North-Holland)

[32] Tokura Y 1999 *Colassal magnetoresistive oxides* (New York: Gordon and Breach Science)

[33] Markovich V, Jung G, Fita I, Mogilyansky D, Wu X, Wisniewski A, Puzniak R, Froumin N, Titelman L, Vradman L, Herskowitz M and Gorodetsky G 2008 *J. Phys. D: Appl. Phys.* **41** 185001

[34] Schiffer P, Ramiraz A P, Bao W and Cheong S W 1995 *Phys. Rev. Lett.* **75** 3336
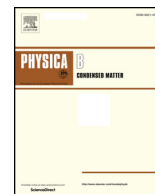
Magnetic and electrical transport of the cation-deficient LaMnO₃: Common origin for both Sr-doping and self-doping effects

S. Das[a], P. Roychowdhury[b], S. De[c], A. Roy[d], S. Chatterjee[c], K. De[b],*

[a] Department of Electronics and Communication Engineering, Guru Ghasidas Central University, Bilaspur, CG 495 009, India
[b] Neotia Institute of Technology, Management and Science, Jhinga, D.H. Road, 24 Pgs (S), 743 368, India
[c] UGC-DAE Consortium for Scientific Research, Kolkata Centre, Sector III, LB-8, Salt Lake, Kolkata 700 098, India
[d] Bratachari Vidyasram (H.S.), Joka, Thakurpukur, Kolkata 700 104, India

ARTICLE INFO

ABSTRACT

We have investigated the effect of cation deficiency on the electric and magnetic properties of LaMnO₃ in terms of both substitution of La by a divalent ion (Sr^{2+}) and creating La-deficiency. The temperature and magnetic field dependence of electrical resistivity (ρ) and dc magnetization were studied. All the compounds are to be found in rhombohedral structure. The excess oxygen in all compounds was detected through iodometric titration. The metal to semiconducting transition and the paramagnetic to ferromagnetic transition is found to decrease with Mn^{4+} for all samples. The occurrence of magnetoresistance (MR) at low temperature and low field for La-deficient compounds is suggested due to the tunneling of electron through the grain boundary (GB). The nonlinear current-voltage (*I–V*) characteristic for La-deficient compounds indicates inelastic tunneling via localized states dominate the transport mechanism.

1. Introduction

Lanthanum-based manganite perovskites exhibiting colossal magnetoresistance (CMR) have attracted great attention in recent years [1,2]. The presence of Mn^{3+} and Mn^{4+} ions together with the site-site double-exchange (DE) mechanism [3] play pivotal role towards such CMR effect. Since in manganites the ferromagnetism (FM) is correlated with the metallic properties and CMR effect, the origin of FM and the possibility to control it are of profound interest. The FM and metal-like behavior observed in hole-doped manganites results usually from a substitution of La sites, by divalent ions such as Sr^{2+}, in the undoped parent compound LaMnO₃ [4–6]. Self-doped lanthanum manganite $La_{1-x}MnO_3$ exhibits magnetic and electrical transport properties very similar to the hole doped manganites where Mn^{4+} appears due to the self-doping [7–11]. Similar to the hole doping, variation of Mn^{4+} leading to the spectacular changes in the physical properties of self-doped lanthanum manganite. The amount of Mn^{3+}/Mn^{4+} ratio and their distribution in the lattice as well as the nonstoichiometric oxygen (creating the equivalent vacancies in La and Mn-sites) plays an important role in tuning the physical properties of these compounds.

For low-doped compositions, the superexchange interaction between the Mn^{3+} ions is responsible for the appearance of FM and/or antiferromagnetic (AFM) insulating phases. The Jahn-Teller (JT) coupling plays an important role leading to the orbital ordering of Mn^{3+} ions and determining also the sign of exchange coupling in accordance with degree of static deformation of the MnO_6 octahedra [12]. The magnetic phase separation occurs with increasing doping, as a result of competition between different kinds of interactions in the system, leading to a mixed AFM-FM ground state. The existence of Mn^{4+} can be achieved by both the substitution of La by a divalent ion as well as creating La-deficiency [13,14]. These changes give evidence of direct correlation among magnetic, structural and electrical properties; namely, the magnetic behavior of the system. This magnetic behavior evolves from AFM to FM with a reduction of JT distortion in the MnO_6 sublattic when structural symmetry changes from the orthorhombic to the rhombohedral [15–18], and when an electron is allowed to hop between Mn^{3+} and Mn^{4+} ions producing a ferromagnetic DE interaction [3], which also promotes a metallic electric conduction.

Until now, no comparative studies have been carried out on cation-deficiencies of LaMnO₃ in terms of both the substitution of La by a divalent ion and creating La-deficiency. We have studied two types of samples: one type was prepared by Sr doping (degree of Sr doping = 10%, 5%, 0%) on self-deificient La-site and another one with Sr doping (degree of Sr doping = 5%) on La-site of stoichiometric compound, LaMnO₃, resulting the variation of Mn^{4+} concentration of both type of samples. In the present paper, we are going to focus on the

---

* Corresponding author.
E-mail address: kalyanashis.de@gmail.com (K. De).

evolution of structural, electrical and magnetic properties with the changes in the Mn^{4+} concentration in cation-deficient compounds by creating vacancies in La-site and/or substitution of La-site by a Sr ($\leq 10\%$).

2. Experimental details

Polycrystalline compounds of nominal composition (a) $[La_{0.9}Sr_{0.1}]_{0.9}MnO_3$, (b) $[La_{0.95}Sr_{0.05}]_{0.9}MnO_3$, (c) $La_{0.9}MnO_3$ and (d) $La_{0.95}Sr_{0.05}MnO_3$ were prepared by a chemical route described in our earlier report [19,20]. The final heat treatment was performed at 800 °C for 15 h in air, followed by furnace cooling to room temperature. In order to remove the ambiguity ascribed to the different oxygen non-stoichiometry, the sample was finally annealed under close oxygen atmosphere for 6 h at 1000 °C. Henceforth, we will refer the samples, denoted with La-site deficiency, by their respective degree of Sr substitution on La-site such as $[La_{0.9}Sr_{0.1}]_{0.9}MnO_3$ as DSr–10%, $[La_{0.95}Sr_{0.05}]_{0.9}MnO_3$ as DSr–5% and $La_{0.9}MnO_3$ as DSr–0%, and the remaining La-stoichiometric compound $La_{0.95}Sr_{0.05}MnO_3$ will be designated by only the respective degree of Sr substitution as Sr–5%. The single phase of compounds was confirmed by the powder X-ray diffraction (Seifert XRD 3000 P) using CuK_α radiation. The size and morphology of the grains of the samples were observed in a JEOL JSM 35 C scanning electron microscope (SEM). Oxygen nonstoichiometry for all samples were checked through iodometric titration as the average of 5 titration values giving the excess oxygen $\approx 1.5\%$. The resistivity (ρ) and MR were measured by the standard four-probe technique in an electromagnet and a commercial closed cycle refrigerator operating down to 10 K (Janis Research Inc.). All the thermal variation during resistivity measurements was carried out at a fixed rate of 2 K/min. DC Magnetization was measured in vibrating sample magnetometer (VSM) with a field range from 0 to 10 T. In case of zero-fieldcooled (ZFC) mode the sample was cooled down to the desired temperature at zero magnetic field while for the field-cooled (FC) mode the sample was cooled in a static magnetic field.

3. Experimental results and discussions

SEM images of studied compounds DSr–10%, DSr–5%, DSr–0% and Sr–5% are shown in Fig. 1(a)-(d), respectively, which clearly show melted grain boundaries. The grains exhibit inhomogeneity in size with average diameter ≈ 170, ≈ 160, ≈ 230 and ≈ 120 nm for the
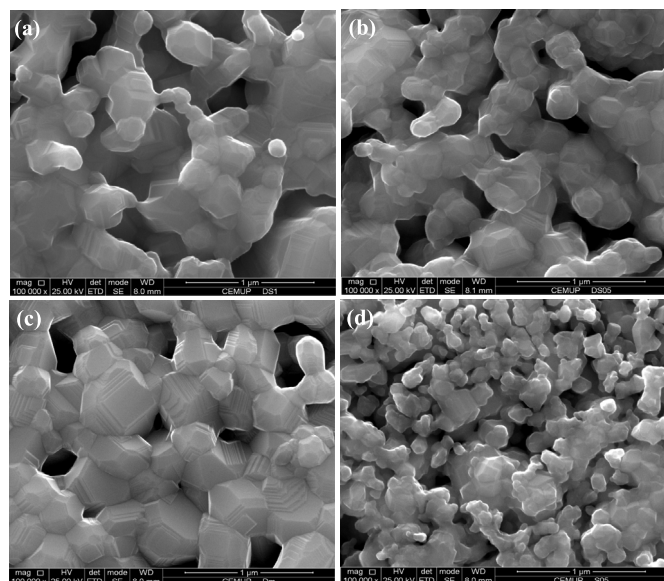

Fig. 1. SEM image of (a) DSr–10% (b) DSr–5% (c) DSr–0% and (d) Sr–5%.

Table 1
Some selected refined structural parameters Obtained from the Rietveld Refinement of the Room Temperature Structure of compounds DSr − 10%, DSr − 5%, DSr − 0% and Sr − 5%.

Parameters	rhombohedral, $R\bar{3}c$			
	DSr − 10%	*DSr − 5%*	*DSr − 0%*	*Sr − 5%*
a (Å)	5.518(3)	5.515(3)	5.522(2)	5.513(4)
c (Å)	13.367(5)	13.358(2)	13.357(6)	13.336(2)
V (Å^3)	352.53(6)	351.92(8)	352.76(8)	351.07(7)
χ^2	2.440(1)	2.683(6)	2.568(8)	2.266(6)
Mn−O (Å^2)	1.944(1)	1.945(6)	1.952(6)	1.941(3)
Mn−O−Mn (deg)	178.51(5)	173.76(8)	169.43(3)	178.51(4)
Mn−Mn (Å)	3.887(7)	3.885(5)	3.888(6)	3.882(4)

compounds DSr − 10%, DSr − 5%, DSr − 0% and Sr − 5%, respectively.

The crystal structure of the systems were analyzed by Rietveld refinement (using the MAUD software package) of XRD data. The Rietveld analysis show that these compounds form in a single phase rhombohedral symmetry with space group $R\bar{3}c$. The refinement was also performed in considering orthorhombic symmetry with space group *Pnma*. However, The agreement factor, χ^2 was significantly improved (Table 1) when rhombohedral symmetry with space group $R\bar{3}c$ was introduced. This structural analysis is in support of the undoped mother sample $LaMnO_3$ [19]. Fig. 2 displays Rietveld fitted XRD patterns of four compounds DSr − 10%, DSr − 5%, DSr − 0% and Sr − 5%, respectively. The selected refined structural parameters and agreement factors are given in Table 1. We did not observe any systematic change of lattice parameters and unit cell volumes with variation of Sr-concentration. Merely, lattice parameter 'c' decreases systematically with Sr-concentration for La-deficient samples. It is also observed that the Mn−O−Mn bond angle decreases with Sr-concentration except stoichemetric sample (Sr–5%). However, the variation of bond angle is understood by considering the valence state of Mn ion. The percentage of Mn^{3+} ion increases with decreasing Sr^{2+} in La-defficient samples to neutralized the charge. Progressively, the larger Mn^{3+} ions replace
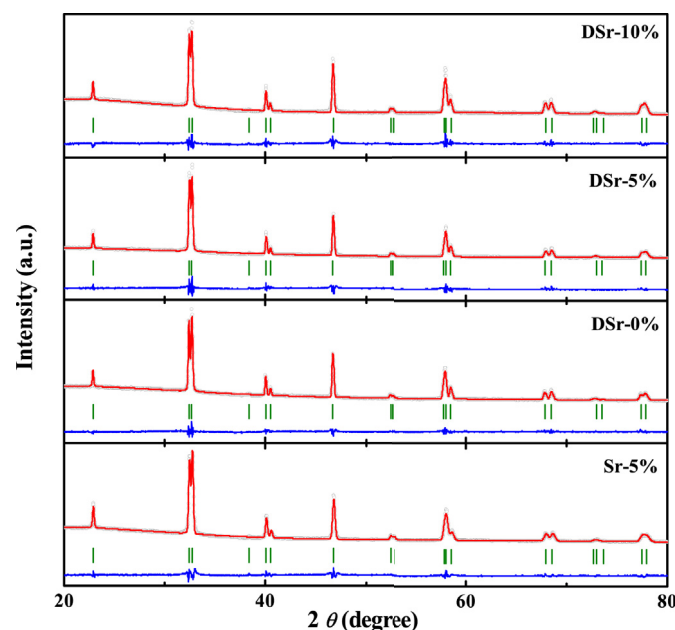

Fig. 2. Experimentally observed (dots), Rietveld calculated (continuous line), and their difference (continuous bottom line) profiles for DSr–10%, DSr–5%, DSr–0% and Sr–5% at room temperature obtained after Rietveld analysis of the XRD data using rhombohedral space group $R\bar{3}c$. The vertical tick marks between the observed and difference plots show the Bragg peak positions.
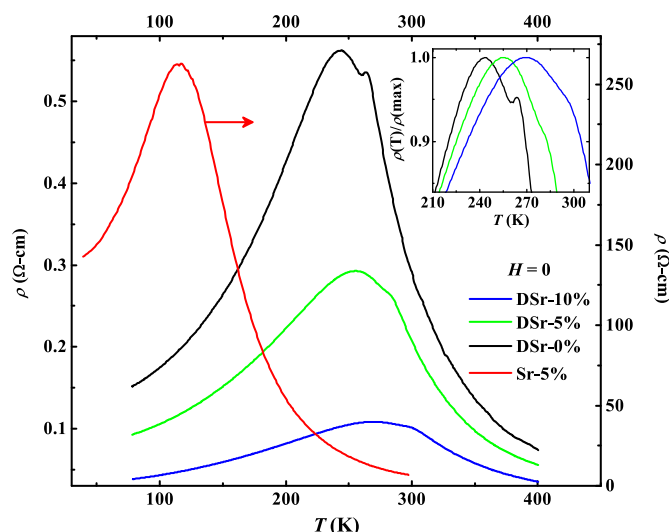
Fig. 3. Temperature dependence of resistivity (ρ) in zero field for DSr–10%, DSr–5%, DSr–0% and Sr–5%. The inset exhibits the temperature dependence of ρ(T)/ρ(max) in a selective temperature region.

smaller Mn^{4+} ions, shearing corners in MnO_6 octahedra resulting the decrease in average $Mn-O-Mn$ bond angle. Such peculiar change in bond angle is also observed earlier in manganites [21–23].

The temperature variation of resistivity (ρ) in zero field is shown in Fig. 3 for the compounds $DSr - 10\%$, $DSr - 5\%$, $DSr - 0\%$ and $Sr - 5\%$, respectively. All the four compounds exhibit insulator-metal (I-M) transition at different temperature region. In comparison to pure $LaMnO_3$, the resistivity is decreased by an order of 3 (i.e. from KΩ-cm to Ω-cm) for all the doped samples [19]. Also the metal-insulator transition temperature which was absent in $LaMnO_3$ [19], now appears in all the four doped samples as seen in Fig. 3. The Mn^{4+} concentration (Table 2) for all compounds has strong effect in their ρ(T)data, which is clearly visible from Fig. 3. A broad maximum appeared around 115 K (T_m) for Sr–5%. The different ρ(T) behavior of Sr–5% has been explained in our previous report [24,25]. On the other hand, a sharp peak is observed at 264 K (T_p) accompanied by a broad maximum around ≈ 243 K (T_m) for DSr–0% (inset of Fig. 3). The features of ρ(T) for DSr–0% is consistent with the previous result where the T_p is 4 K higher than the reported result [9,10,26]. The similar temperature dependence of ρ is also noticed for $DSr - 5\%$ and $DSr - 10\%$. Inset of Fig. 3 shows that the sharp peak at T_p becomes less prominent and shifts towards higher temperature at $T_p = 280$ and 293 K for $DSr - 5\%$ and $DSr - 10\%$, respectively. In addition with T_P, the width of broad

Table 2
Mn^{+4} (%); Sharp maximum in ρ(T), (T_p); Broad maximum in ρ(T), (T_m); Curie temperature (T_C); Curie-Weiss temperature (Θ_W); Effective magnetic moment from the Curie–Weiss plot (μ_{eff}); Theoretical effective magnetic moment (μ_{eff}^{th}); Saturation magnetic moment at 5 K (μ_{sat}); Theoretical Saturation moment (μ_{sat}^{th}) for compounds DSr–10%, DSr–5%, DSr–0% and Sr–5%.

Sample	DSr–10%	DSr–5%	DSr–0%	Sr–5%
Mn^{+4} (%)	39	33.5	30	5
T_p (K)	293	280	264	–
T_m (K)	263	255	243	115
ρ_{400K} (Ω–cm)	0.035	0.056	0.074	0.144
T_C (K)	303	290	265	$T_{C1} = 290$ K $T_{C2} = 150$ K
Θ_W (K)	303	290	265	283
μ_{eff}(μ_B/f.u.)	4.85	4.83	4.80	3.25
μ_{eff}^{th}(μ_B/f.u.)	4.53	4.57	4.61	4.85
μ_{sat}(μ_B/f.u.)	3.65	3.83	3.69	2.91
μ_{sat}^{th}(μ_B/f.u.)	3.64	3.68	3.71	3.95

maximum increases with increasing Sr-concentration and T_m is noticed ≈ 255 and ≈ 263 K for DSr −5% and DSr − 10%, respectively. The appearance of a sharp peak (T_p) and a broad maximum (T_m) is attributed to the inhomogeneity of the oxygen stoichiometry in different phases in the samples, where the oxygen-rich phase is responsible for the appearance of sharp peak in ρ(T) [9,10,26]. It is interesting to note that the increase of Mn^{4+} concentration leads to a metal like temperature dependence (dρ/d$T \geq 0$) and the absolute value of ρ at 400 K (ρ_{400K}) decreases with increasing Mn^{4+} percentage for all samples which is listed in Table 2. As a result of La deficiency in DSr − 0%, the onset oxidation state of Mn changes from Mn^{3+} to 30% Mn^{4+}. Furthermore, Sr^{2+} substitution implants more Mn^{4+} in the Mn^{3+} matrix. Both La deficiency as well as doping divalent Sr onto the trivalent La sites results in hole doping (Mn^{4+}) and the eventual onset of metallic behavior. The percentage of Mn^{4+} of all samples is shown in Table 2. It is widely accepted [27,28] that the current carriers in hole doped ($La_{1-x}A_xMnO_3$) and self doped ($La_{1-\delta}MnO_3$) manganites, at least at moderate x and δ, are mobile holes, which appear due to charge compensation and move from Mn^{4+}ions to normal-valence Mn^{3+} ions. These holes simultaneously dominate the metallic transport and mediate the FM double-exchange(DE) interaction.

Fig. 4 shows the temperature (T) dependence of magnetization (M) measured at 100 Oe in ZFC and FC protocols for DSr–10%, DSr–5%, DSr–0% and Sr–5%. The compounds DSr − 10%, DSr − 5%, DSr − 0% show typical ferromagnetic behavior. However, for stoichemetric compound Sr − 5%, the $M - T$ behavior is quite different. The distinct magnetic response of Sr − 5% was explained by an unusual ferromagnetic ordering which dominated this system over a wide temperature range as reported previously [24,25]. The Sr-concentrations on La-deficient samples are found to affect magnetic behavior. A sharp ferromagnetic transition is observed for all La-deficient samples. Large thermomagnetic irreversibility between ZFC and FC data below T_C in Fig. 4 arises either from the magnetic anisotropy [29] or due to spin-glass-like behavior [30]. The magnetization curves at 5 K in Fig. 5 exhibit soft ferromagnetic features for all La-deficient compounds and thus the possibility of spin-glass-like feature has been ruled out. A sharp PM to FM transition is observed at T_C, as obtained from the deep in the plot of temperature derivation of FC magnetization (dM_{FC}/dT) with T, where M_{FC} is the FC magnetization. T_C for all the compounds is shown in Table 2. In comparison to $LaMnO_3$, T_C increase closed to room temperature approximately from 140 K (for $LaMnO_3$) [19].

We have examined the plot of inverse susceptibility (H/M) with temperature which follows a linear behavior above T_C, in the measured
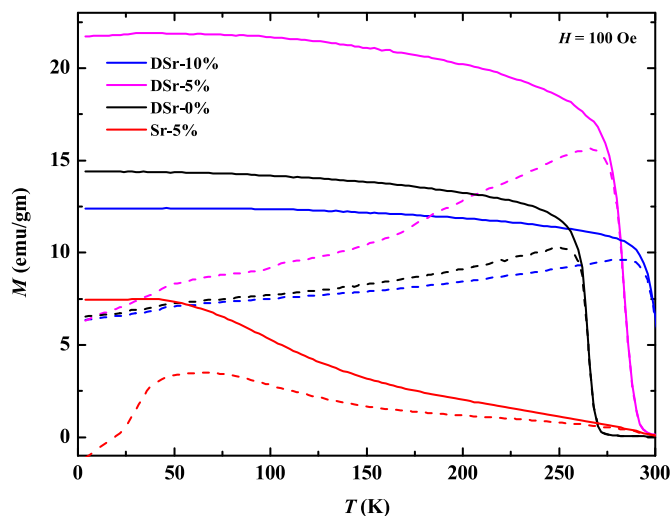

Fig. 4. Temperature dependence of ZFC (dotted lines) and FC (solid lines) magnetization in an applied field of 100 Oe for DSr–10%, DSr–5%, DSr–0% and Sr–5%.
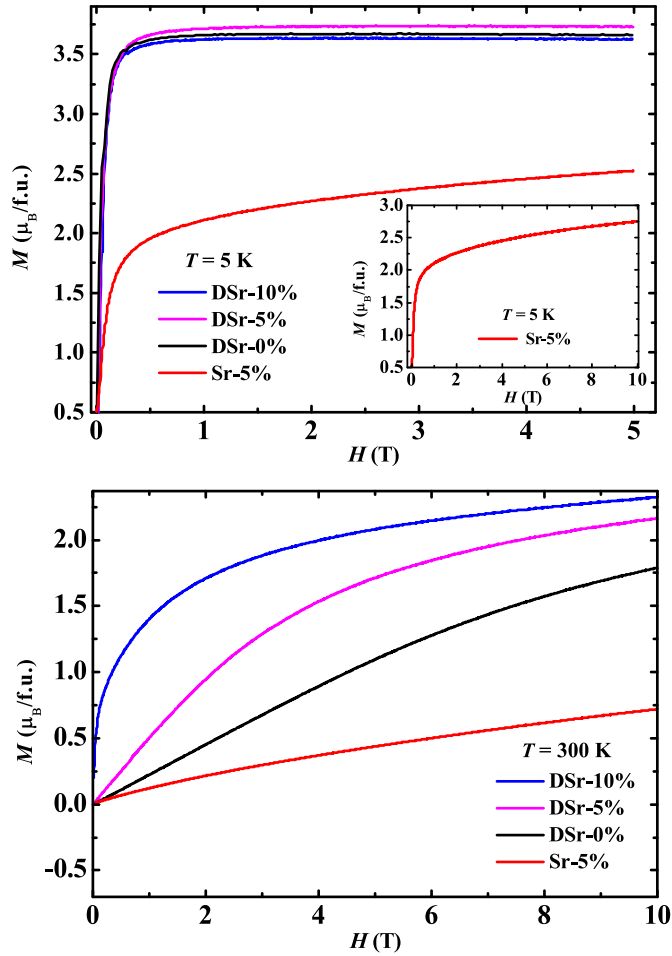
Fig. 5. Magnetization as a function of applied field for DSr − 10%, DSr − 5%, DSr − 0% and Sr − 5% measured at different temperatures. The inset of the top panel exhibits the extended view of the same for Sr − 5% at 5 K up to 10 T.

range up to 330 K, according to the Curie-Weiss law: $M/H = C/(T - \Theta_W)$, where C and Θ_W are the Curie and Weiss constant, respectively. The obtained value of the effective paramagnetic moment (μ_{eff}) and Θ_W are shown in Table 2. The value of Θ_W is in good agreement with Curie temperature (T_C) for all the samples. The values of μ_{eff} can be compared to that obtained from the theoretical model [31,32]. Considering the rigid Hund coupling within Mn^{3+} and Mn^{4+} in their high spin state, the theoretical effective paramagnetic moment (μ_{eff}^{th}) per formula unit can be estimated and listed in Table 2. Note that the value of μ_{eff} for all La deficient samples (DSr–10%, DSr–5%, DSr–0%) is about ≈10% larger than the theoretical provided values while that for Sr–5% is ≈15% lower than it. Considering the presence of almost same amount of excess oxygen (less than 2%) in these compounds, the larger value of μ_{eff} in La deficient samples indicates a probable existence of FM cluster [7,8,19]. The presence of surface disordered effect at the grains and/or magnetic clustering counts for lower value of μ_{eff} for Sr − 5% [24,25]. It is worth to note that the large value of μ_{eff} (6.07 μ_B/f.u.) for pure LaMnO$_3$ compared to the spin only value for $S = 2$ (4.90 μ_B/f.u.) suggests the existence of superparamagnetic clusters, where the inside interaction is ferromagnetic [19]. With increasing Mn^{4+} content the value of T_C shifted towards higher temperature. T_C for DSr − 0% was estimated at 265 K which coincides the value of T_p in temperature dependence of ρ. It is understood that increasing Mn^{4+} content with Sr content as well as La deficiency commits the hole-rich ferromagnetic phases dominated by the ferromagnetic double exchange interaction between Mn^{4+} and Mn^{3+}.

The isothermal magnetization of the compounds is measured as a

function of field at 5 and 300 K and is shown in Fig. 5. All the data were recorded after cooling the sample from 400 K and then stabilized at 5 and 300 K. Except for the sample Sr − 5%, at 5 K, magnetization initially increases rapidly with H and saturates at ≈1.0 T, indicating the characteristic features of soft ferromagnet for all La-deficient samples. However, the magnetic saturation is not observed for Sr − 5% with the applied magnetic field up to the 5 T. The inset of the top panel of Fig. 5 shows that the rate of increase of M with H decreases in the high magnetic field region (2 T ≤ H ≤ 10 T) and no saturation is observed even at 10 T. The value of saturation magnetic moments (μ_{sat})was calculated from the magnetic moment extrapolated at $1/H = 0$ in the plot of M vs $1/H$ at 5 K μ_{sat} of Sr − 5% shows a large deviation from μ_{sat}^{th} explaining the presence of antiferromagnetic interactions accompanying with cluster/spin glass (SG) behavior [24,25]. μ_{sat} at 5 K and 5 T are listed in Table 2. The value of μ_{sat} suggests the oxygen stoichiometry ≈3 for DSr − 0%, and is consistent with reported result [8]. The relatively small value of μ_{sat} (also μ_{sat}^{th}) in DSr–10% compared to that of DSr–0% is a measure of Mn^{4+} doping in this compound however for DSr–5%, the value of μ_{sat} comes out much higher than that of corresponding μ_{sat}^{th}. This difference suggests that the system with DSr −5% is having a probable presence of Mn^{2+} (in high spin state) along with Mn^{4+} however our X-ray diffraction did not show the existence of any multi-phase structure for this compound. The high value of μ_{sat} for DSr −5% is therefore anomalous and needs to be probed further. The nonlinearity of M–H curve at 300 K (the lower panel of Fig. 5) for DSr − 10%, DSr − 5%, DSr − 0% might be ascribed to the presence of short range FM clusters at 300 K satisfying Curie–Weiss behavior. At 300 K for Sr − 5%, i.e., above T_C, the quasi-linear M(H) curve is the indication of paramagnetic nature of sample at that temperature.

We observed the nature of low-field MR at selected temperatures by varying the magnetic field up to ± 8.5 kOe for DSr − 5% and DSr − 10%. The plots of MR are shown in Fig. 6, exhibiting different characteristic features at different temperatures for DSr − 5% and DSr − 10%. The nature of MR-H curves at 40 and 150 K are similar, while at 40 K, we observed 24% MR value at 8.5 kOe field for DSr − 5% (top panel of Fig. 6). In the bottom panel of Fig. 6 shows the similar nature of MR-H curves at 55, 153 and 201 K for DSr − 10% and the maximum value of MR estimates 23% at 55 K and 8.5 kOe of applied field. The linear variation of MR with H is shown around the T_C at 290 and 303 K for DSr − 5% and DSr − 10%, respectively. MR increases monotonically with decreasing temperature indicating the feature of spin tunneling through the grain boundary (GB) region [33]. Similar low-field MR behavior was also observed for DSr − 0% and Sr − 5% as reported earlier [24,33].

In order to understand the electronic transport mechanism at low temperature that involves tunneling across the GB, the current-voltage (I–V) curves were measured at selective temperatures in zero magnetic field. The nonlinear I–V characteristic of DSr −0% was reported in our early study [33] and interpreted in terms of inelastic tunneling via localized states. The I–V curves of DSr − 5% are qualitative similar to the curves which were taken for DSr − 10%, although they differ in quantitative details. However, to avoid duplicity the data for DSr − 5% is not given. In contrast, the linear I–V characteristic of Sr − 5% has been examined where ohmic conductivity is observed up to ± 2 V as shown in lower inset of bottom pannel og Fog. 7. The signature of nonlinear curves at selective temperatures for DSr − 10% in the range 48–300 K are shown in the inset of top panel of Fig. 7. The nonlinearity of I–V curves at different temperatures are depicted in top panel of Fig. 7 through the dynamic conductance, G(V, T) for $T ≤ T_C$ where G(V, T) is defined as dI/dV which is obtained by the numerical differentiation of the I–V curves. The weight of nonlinear transport is investigated by fitting the voltage dependent conductance at different temperatures to the phenomenological relation [34].

$$G(V, T) = G_0(T) + G_\alpha(T)|V|^\alpha \qquad (1)$$

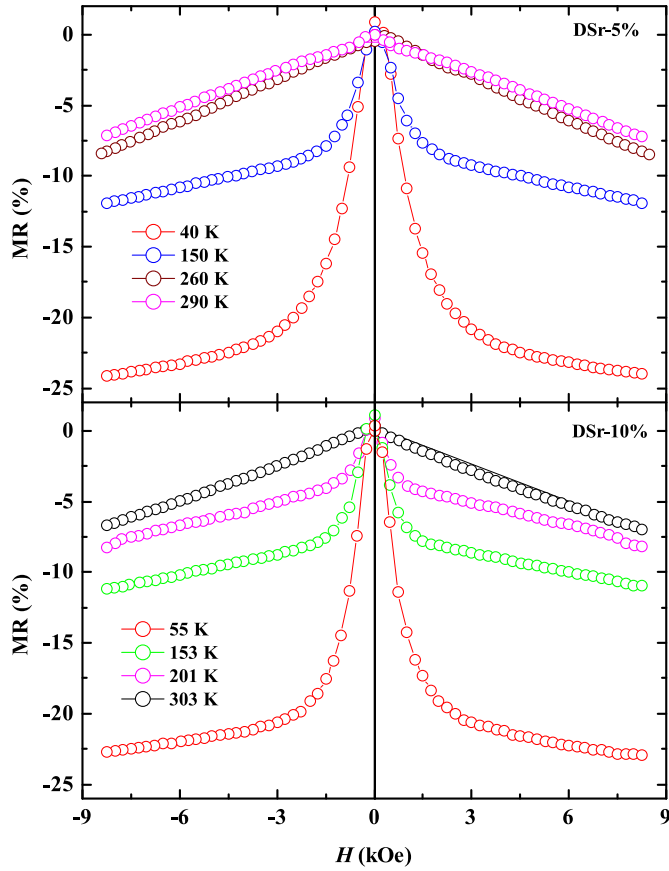where the nonlinearity is interpreted through the conductance

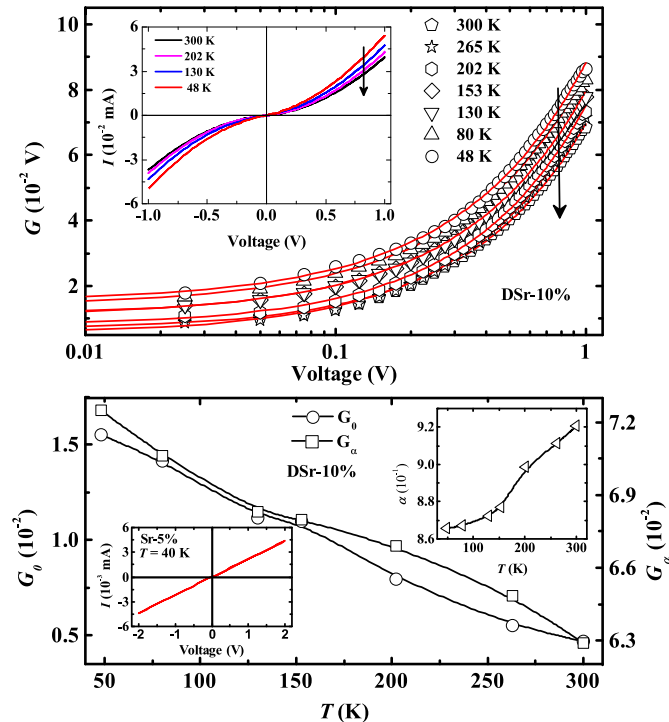**Fig. 6.** MR as a function of field (H) at selective temperatures for DSr–5% and DSr–10%.

Fig. 7. Top panel: G_V–V curves at selective temperatures. The solid lines exhibit the fits using Eq. (1). Inset exhibits I–V curves at selective temperatures. Bottom panel: The temperature dependence of the coefficients G_0 and G_α are obtained from Eq. (1). Upper inset shows the temperature dependence of α. Lower inset shows I–V curve for $Sr - 5\%$.

exponent, α and the weight factor, G_α. G_0 denotes the conductance in the zero voltage limit. Eq. (1) has been used extensively to interpret the nonlinear transport in manganites [34–37]. We fit the observed $G(V, T)$–V data for DSr–10% to Eq. (1) over the whole voltage range and at all temperatures (48–300 K). One can obtain excellent fit using Eq. (1). Bottom panel of Fig. 7 shows the temperature dependence of the three parameters obtained from the fits. G_0 and G_α decrease monotonically with increasing temperature. The obtain fitted parameters, G_α and G_0 varied from 0.07251 to 0.06291 and 0.01553 to 0.00471, respectively. However, α increases monotonically from 0.86553 at 48 K to 0.9206 at 300 K which is shown in the upper inset of bottom panel of Fig. 7. The variation of $\alpha(T)$ is more steeper at the high temperature region ($153\,K \leq T \leq 300\,K$). In the case of direct elastic tunneling through the GB barrier, the exponent α equals to 2 at low voltages described by the quantum tunneling theory of Simmons [38]. If the transport is dominated by the inelastic tunneling via localized states at GB, Glazman and Matveev [39] predicted that α is nonquadratic. Recently, from the investigation in bulk $La_{0.9}MnO_3$ a value of $\alpha = 1.25$–1.5 suggested that inelastic tunneling via localized states is dominant in transport mechanism at low temperatures [33]. The dependence of G_α and α with temperature indicates that the nonlinear I–V behavior in same biasing voltage increases with increase of temperature in the entire temperature range. The temperature and field dependence of α, G_α and G_0 suggest that the inelastic tunneling via localized states is dominant in the transport mechanism.

4. Conclusions

The low temperature metallic behavior with a characteristic feature of metal to semiconducting transition accompanying with a typical feature of FM character are observed for all compounds. The compound with $Sr - 5\%$ shows different characteristic features such as two FM ordering temperatures at T_{C1} and T_{C2}, absence of sharp peak at T_p in $\rho(T)$, and linear ohmic I–V behavior below T_C. Increasing Mn^{4+} content with Sr content as well as La deficiency commits the hole-rich FM and metallic phases. The distinct behavior of low field MR below T_C is suggested due to the tunneling of electrical transport across the GB region. The analysis of the nonlinear current-voltage curves for La deficient samples further indicates that the inelastic tunneling via localized states of the GB region is dominant.

References

[1] Y. Tokura, N. Nagaosa, Science 288 (2000) 462.
[2] E. Dagotto, T. Hotta, A. Moreo, Phys. Rep. 344 (2001) 1.
[3] C. Zener, Phys. Rev. 82 (1951) 403.
[4] A. Urushibara, Y. Moritomo, T. Arima, A. Asamitsu, G. Kido, Y. Tokura, Phys. Rev. B 51 (1995) 14103.
[5] S. Nair, A. Banerjee, A.V. Narlikar, D. Prabhakaran, A.T. Boothroyd, Phys. Rev. B 68 (2003) 132404.
[6] Y. Endoh, K. Hirota, S. Ishihara, S. Okamoto, Y. Murakami, A. Nishizawa, T. Fukuda, H. Kimura, H. Nojiri, K. Keneko, S. Maekawa, Phys. Rev. Lett. 82 (1999) 4348.
[7] S. de Brion, F. de Ciorcas, G. Chouteau, P. Lejay, P. Radaelli, C. Chaillout, Phys. Rev. B 59 (1999) 1304.

[8] I.O. Troyanchuk, V.A. Khomchenko, M. Tovar, H. Szymczak, K. Barner, Phys. Rev. B 69 (2004) 054432.

[9] K. De, S. Majumdar, S. Giri, J. Phys. Condens. Matter 19 (2007) 096205.

[10] K. De, S. Majumdar, S. Giri, J. Phys. D: Appl. Phys. 40 (2007) 5810.

[11] M. Patra, K. De, S. Majumdar, S. Giri, Appl. Phys. Lett. 94 (2009) 092506.

[12] I. Solovyev, N. Hamada, K. Terakura, Phys. Rev. Lett. 76 (1996) 4825.

[13] S. Wang, S. Du, W. Tang, S. Hoang, X. Lu, W. Xiao, B. Zhang, J. Weng, E. Schneer, Y. Guo, J. Ding, Z. Zhang, P. Gao, ChemCatChem (2018), http://dx.doi.org/10. 1002/cctc.201702048.

[14] M. Pavone, A.B. Muñoz-García, A.M. Ritzmann, E.A. Carter, J. Phys. Chem. C 118 (25) (2014) 13346.

[15] C. Ritter, M.R. Ibarra, J.M. De Teresa, P.A. Algarabel, C. Marquina, J. Blasko, J. Garcia, S. Oseroff, S.-W. Cheong, Phys. Rev. B 56 (1997) 8902.

[16] J. Töpfer, J.B. Goodenough, J. Solid State Chem. 130 (1997) 117.

[17] F. Prado, R.D. Sánchez, A. Caneiro, M.T. Causa, M. Tovar, J. Solid State Chem. 146 (1999) 418.

[18] M. Muroi, R. Street, Aust. J. Phys. 52 (1999) 205.

[19] K. De, R. Ray, R.N. Panda, S. Giri, H. Nakamura, T. Kohara, J. Magn. Magn Mater. 288 (2005) 339.

[20] K. De, A. Roy, C.J.R. Silva, M.J.M. Gomes, Solid State Commun. 150 (2010) 1187.

[21] J.-S. Kang, Y.J. Kim, B.W. Lee, C.G. Olson, B.I. Min, J. Phys. Condens. Matter 13 (2001) 3779.

[22] M.S. Kim, J.B. Yang, Q. Cai, X.D. Zhou, W.J. James, W.B. Yelon, P.E. Parris, D. Buddhikot, S.K. Malik, Phys. Rev. B 71 (2005) 014433.

[23] K.R. Mavani, P.L. Paulose, Phys. Rev. B 72 (2005) 104421.

[24] K. De, S. Das, A. Roy, P. Dhak, M. Willinger, J.S. Amaral, V.S. Amaral, S. Giri, S. Majumder, C.J.R. Silva, M.J.M. Gomes, P.K. Mahapatra, J. Appl. Phys. 112 (2012) 103907.

[25] S. Das, J.S. Amaral, K. De, M. Willinger, J.N. Goncalves, A. Roy, P. Dhak, S. Giri, S. Majumder, C.J.R. Silva, M.J.M. Gomes, P.K. Mahapatra, V.S. Amaral, Appl. Phys. Lett. 102 (2013) 112408.

[26] K. De, S. Majumdar, S. Giri, J. Magn. Magn Mater. 322 (2010) 337.

[27] J.M.D. Coey, M. Viret, S. von Molnar, Adv. Phys. 48 (1999) 167.

[28] E. Dagotto, T. Hotta, A. Moreo, Phys. Rep. 344 (2001) 1.

[29] D.C. Kundaliya, R. Vij, R.G. Kulkarni, A.A. Tulapurkar, R. Pinto, S.K. Malik, W.B. Yelon, J. Magn. Magn Mater. 264 (2003) 62.

[30] K. De, M. Patra, S. Majumdar, S. Giri, J. Phys. D: Appl. Phys. 40 (2007) 7614.

[31] F. Millange, S. de Brion, G. Chouteau, Phys. Rev. B 62 (2000) 5619.

[32] A. Biswas, I. Das, J. Appl. Phys. 102 (2007) 064303.

[33] M. Patra, A. Roy, K. De, S. Majumdar, S. Giri, Appl. Phys. Lett. 94 (2009) 212107.

[34] M. Ziese, Phys. Rev. B 60 (1999) R738.

[35] M. Paranjape, J. Mitra, A.K. Raychaudhuri, N.K. Todd, N.D. Mathur, M.G. Blamire, Phys. Rev. B 68 (2003) 144409.

[36] N. Khare, U.P. Moharil, A.K. Gupta, A.K. Raychaudhuri, S.P. Pai, R. Pinto, Appl. Phys. Lett. 81 (325) (2002).

[37] R. Shao, J. Vavro, D.A. Bonnell, Appl. Phys. Lett. 85 (2004) 561.

[38] J.G. Simmons, J. Appl. Phys. 34 (1963) 1793.

[39] L.I. Glazman, K.A. Matveev, Sov. Phys. JETP 67 (1988) 1276.

De-stabilization of charge-order state through in-homogeneity in random ionic distribution in the particles of polycrystalline Eu$_{0.2}$La$_{0.3}$Sr$_{0.2}$Ca$_{0.3}$MnO$_3$ sample

K DE[1], P DHAK[2], S DE[3], P DUTTA[4], K DEY[4], S MUKHERJEE[5], S CHATTERJEE[3] and S DAS[6,]*

[1]The Neotia University, D.H. Road, 24 Pgs (south), Sarisa 743 368, India

[2]Department of Chemistry, Center for Materials Science and Nanotechnology, 0351 Oslo, Norway

[3]UGC-DAE Consortium for Scientific Research, Kolkata Centre, Kolkata 700 098, India

[4]Department of Solid State Physics, Indian Association for the Cultivation of Science, Jadavpur 700 032, India

[5]UGC-DAE Consortium for Scientific Research, Mumbai Centre, BARC Campus, Mumbai 400085, India

[6]Department of Electronics and Communication Engineering, Guru Ghasidas Central University, Bilaspur, C.G. 495 009, India

*Author for correspondence (soma.iitkharagpur@gmail.com)

Abstract.   In this study the perovskite manganite Eu$_{0.2}$La$_{0.3}$Sr$_{0.2}$Ca$_{0.3}$MnO$_3$ batch integrated sample is studied, with special modification done to introduce localized structural strain without micro-level (grains) modification. This consequence successfully generates opposite nature of high orthorhombic strain along *b*-axis in these samples, although the general structure is same for both with *Pnma* space group. The sharp magnetic transitions (both Curie temperature and charge-order transition) are reported to be mixed in presence of random ionic distribution in its structure. The diffused insulator-metal behaviour, de-stabilization of magnetic state and phase transitions associated with inherent anisotropic strain is discussed and is explained based on chemical disorder-induced structural strain in the present system.

Keywords.   Charge order; in-homogeneity; structural strain.

1. Introduction

The correlation between the structural and magnetic degrees of freedom in doped manganite perovskites generating different fascinating electronic and magnetic state is the subject of interest from the last two decades. The charge-ordered (CO) state of manganites is associated with a real space ordering of Mn^{3+}/Mn^{4+} species in a 1:1 pattern. The modification/de-stabilization of CO state in half-doped manganites becomes the subject of interest due to varieties of controlling parameters like magnetic field, doping, bi-axial strain, pressure, electric field, size reduction, etc. [1–10]. The result presented by Sarkar *et al* [8] showed that size reduction can lead to an arrest of the high temperature phase in perovskite materials, which prevents the growth of low temperature phase that needs a specific crystal structure for its stabilization. Later on, Gutiérrez *et al* [11] showed that large compressive strain triggers a change from a ferromagnetic (FM) and metallic ground state to an insulating and anti-FM state, whereas a tensile strain produces an anti-FM but metallic state. However for some other half-doped manganites, anti-FM insulator state remains unaffected irrespective of the strain state [11]. Again, the influence of disorder and corresponding phase separation on half-doped manganites

due to the broadening of the first-order phase transition region was reported by Chaddah *et al* [12]. Further, the presence of metastability and field-induced arrest around the first-order insulator-metal transition region in half-doped manganites was also reported in literature [13]. The suppression of charge-ordering transition due to the enhanced surface disorder was also reported [7,14]. The disappearance of anti-FM phase and emergence of FM metallic phase in half-doped nanoparticles was reported by Pramanik and Banerjee [15]. This inter-related effects as well as the large number of contradictory experimental reports and theoretical models relating to the properties of these materials with internal in-homogeneity revealed the complexity of the problem demanding more research in this field [9–19].

In order to put further light on this controversial issue on origin of suppression of CO state of manganites, we have selected polycrystalline Eu$_{0.2}$La$_{0.3}$Sr$_{0.2}$Ca$_{0.3}$MnO$_3$ batch integrated sample, which is specially modified by different final heat treatment that introduce unlike-strain in its structure due to chemical disorder (Samples A and B in oxygen atmosphere) without modifying it in micro-level (grains). The general orthorhombic structure with *Pnma* space group is influenced by local chemical disorder in such a way that the nature

of high orthorhombic strain along *b* axis becomes opposite in these two samples. The detailed study on magnetic and transport properties of these samples show that the sharp magnetic transition (both Curie temperature and CO transition) of Sample A is drastically modified in Sample B due to in-homogeneous ionic distribution. The de-stabilization of magnetic state, phase transitions and its behaviour with different chemical disorder for Sample B associated with inherent structural anisotropic strain is discussed. The comparative study of Samples A and B is reported and explained based on chemical disorder-induced structural strain in the present system.

2. Experimental

Polycrystalline $Eu_{0.2}La_{0.3}Sr_{0.2}Ca_{0.3}MnO_3$ was prepared by a chemical process described in our earlier report [20]. The

Figure 1. SEM images of (**a**) Sample A and (**b**) Sample B.

final annealing was performed at 1000°C for 15 h in air followed by furnace cooling to room temperature. One part of the sample was further annealed under closed oxygen atmosphere for 6 h at 1000°C. Henceforth, we will refer the samples by their respective final heat treatment, such as sample annealed at 1000°C in air as Sample A and the remaining sample annealed at 1000°C under closed oxygen atmosphere as Sample B. The single phase of compounds was confirmed by the powder X-ray diffraction (Seifert XRD 3000 P) using CuK_α radiation. The size and morphology of the grains of the samples were observed in a JEOL JSM 35 C scanning electron microscope (SEM). Bulk oxygen homogeneity of both samples was verified through iodometric titration method. The temperature-dependent electrical resistivity (ρ) at different constant applied magnetic fields was recorded using a commercial cryogen-free high-magnetic field system from Cryogenic Ltd, UK. DC magnetic measurements were performed using a Quantum Design SQUID magnetometer (magnetic property measurement system (MPMS) XL 7, Ever-cool model). In case of zero-field-cooled (ZFC) mode, the sample was cooled down to the desired temperature at zero magnetic field, while for the field-cooled (FC) mode the sample was cooled in a static magnetic field.

3. Experimental Results and discussions

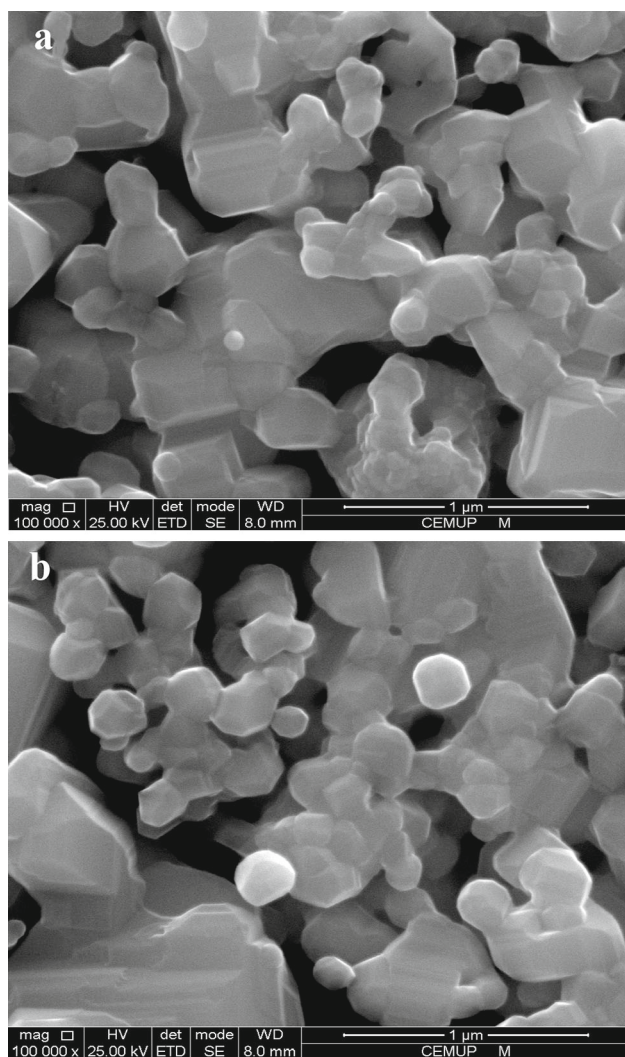The microscopic characterizations of the presently studied compounds were performed through SEM. The SEM images
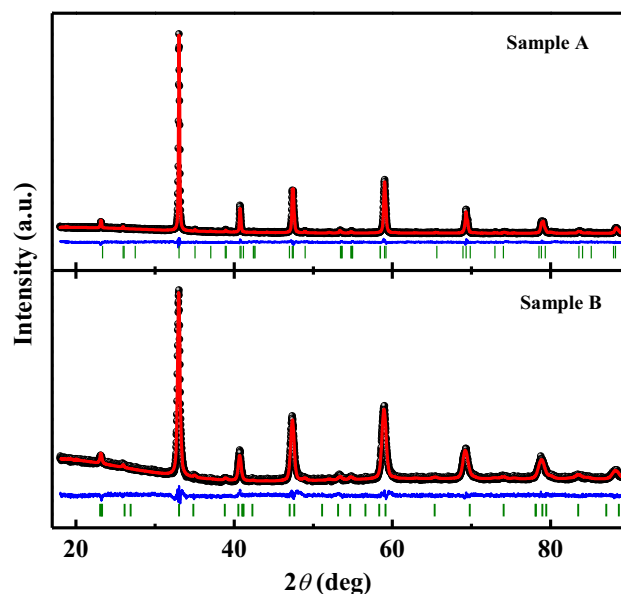

Figure 2. Experimentally observed (dots), Rietveld calculated (continuous line), and their difference (continuous bottom line) profiles for Sample A and Sample B at room temperature obtained after Rietveld analysis of the XRD data using orthorhombic space group *Pnma*. The vertical tick marks between the observed and difference plots show the Bragg peak positions.

of Samples A and B are shown in figure 1a and b, respectively, which show the resolved submicron-sized grains of both the samples with sharp grain boundaries; range of grain sizes are same for both the samples and are estimated from SEM to be ∼200 nm. The particle sizes obtained from X-ray data, using Scherrer formula corresponding to full-width of half-maximum (FWHM) of the major peak, are ≈346 and ≈173 nm for Samples A and B, respectively, which are in good agreement with microscopic results.

Table 1. Some selected refined structural parameters obtained from the Rietveld refinement of the room temperature structure of compounds Sample A and Sample B.

Parameters	Orthorhombic, *Pnma*	
	Sample A	Sample B
A (Å)	5.431 (2)	5.433 (4)
B (Å)	7.651 (1)	7.698 (1)
C (Å)	5.421 (4)	5.409 (3)
V (Å^3)	225.28 (6)	226.25 (4)
χ^2	1.424 (5)	1.481 (6)
Mn–O$_1$ (Å)	1.925 (2)	1.964 (4)
Mn–O$_2$ (Å)	1.762 (1)	1.865 (3)
Mn–O$_1$–Mn (Deg)	166.96 (5)	156.85 (2)
Mn–O$_2$–Mn (Deg)	174.71 (8)	171.77 (3)
Mn–Mn (Å)	3.883 (4)	3.882 (4)

The crystal structures of the studied systems were analysed by Rietveld refinement (using the MAUD software package) of XRD data [21]. Rietveld analysis reveals that both the samples are of orthorhombic structure with *Pnma* space group, which is consistent with the earlier reports [9,16]. Figure 2 shows the Rietveld fits for the room temperature XRD pattern using *Pnma* space group. The selected result of Rietveld analysis is presented in table 1 with refined structural parameters and corresponding bond angles. The striking feature obtained from the Rietveld refinement is the relative difference in lengths of the sides of structure of two samples. The *Pnma* structure is elongated along *b* axis in Sample B by 0.047 Å compared to that in Sample A, which finally yields the orthorhombic strain $OS_\perp = 2(c+a-b\sqrt{2})/(c+a+b\sqrt{2})$ in the structure as $OS_\perp = -0.00411$ (Sample B) compared to $+0.0294$ in Sample A. This opposite nature of strain in structure is a striking feature, as the samples are batch processed ones. The orthorhombic strain $OS_\| = 2(c-a)/(c+a)$ in *ac*-plane is $OS_\| = -0.00184$ for Sample A, which differs from that in Sample B as -0.00443; i.e., the nature of orthorhombic strains is compressive for Sample B both in *ac*-plane as well as perpendicular to *ac*-plane, whereas strain in Sample A is tensile along *b* axis perpendicular to *ac*-plane and compressive in *ac*-plane. Therefore, the difference in ionic distribution in the crystal structures lead in such a way that the Sample B is stressed equally from all sides, which is in contrast to the situation of Sample A. This dissimilarity of structural strains however did not affect the crystal structure and overall symmetry is still maintained as *Pnma*. The remarkable change in side *b* also affects the Mn–O–Mn bond angles between the samples by an amount of 10.11° in Mn–O$_1$–Mn (out of
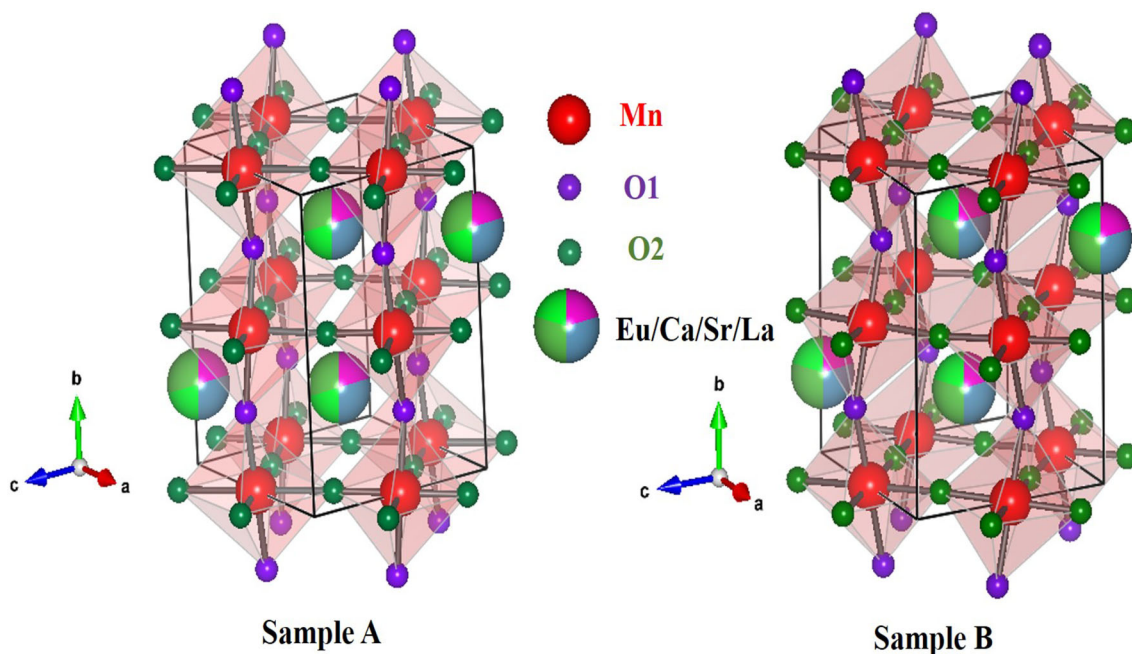

Figure 3. The crystal structure of Samples A and B illustrated schematically.

ac-plane), whereas the difference between Mn–O$_2$–Mn angle between Samples A and B is 2.94°. The large difference in Mn–O$_1$–Mn bond angle between the samples is assisted with the large difference in side *b*, which finally affects the unit cell volume. As obtained from Rietveld analysis, the unit cell volume of Sample A is 225.28 Å^3, which is in support of the already published literatures of these type of half-doped samples, whereas Sample B shows bigger cell volume of 226.25 Å^3 [22]. As reported by Sarkar *et al* [9], OS$_\perp$ significantly increases in the low temperature CO phase. Hence, the high negative value of OS$_\perp$ in Sample B indicates a probable de-stabilization of CO state in this system. Figure 3 shows the 3-dimensional structure of both the samples, where the structural difference between them is clearly visible.

The magnetization measurements are performed in zero-field-cooled heating (ZFCH), field-cooled cooling (FCC) and field-cooled heating (FCH) for both the samples shown in figure 4a and b. As depicted in figure 4a, Sample A shows a transition from paramagnetic (PM) to FM state at $T_C \approx 101$ K and then a nearly flat region followed by a transition to CO state at $T_{CO} \approx 35.5$ K on further lowering of the temperature during ZFCH protocol. The decrease of magnetization values with decreasing temperature is maintained even after T_{CO} but with different gradient denoting magnetic phases with different energy barrier present in the system at low temperature. However, the FCC and FCH curves do not resemble this ZFCH nature and a flat region is observed below 50 K inferring the presence of strong competition between FM and AFM phases. Prominent thermal hysteresis is present in magnetization curve (FCC and FCH) of Sample A, which clearly indicates the first-order nature of the transition in the Sample (figure 4a). In Sample B, the nature of ZFCH magnetization follows the same trend. However, the observed peak-like feature in ZFCH data is more broad than Sample A. This broad hump in the ZFCH curve of Sample B symbolizes the presence of mixed PM phases in the system. Therefore, the observed T_C of Sample B ($\sim$215 K) is found to be much higher compared to that in Sample A. The flattened region over a broad temperature range below T_C is a signature of heterogeneous as well as weak CO state, resulting in the CO transition not in one temperature but in series of points at $T_{CO} \approx 77, 38$ and 11 K, respectively. The relative difference in the nature of thermal hysteresis between FCC and FCH curves for these two samples indicate the random distribution of different mixed magnetic phases in the system influenced by the chemical disorder. This is also associated with the relative difference in the structural parameters giving such differences in their behaviour.

The effective theoretical magnetic moment (μ_{th}^{eff}) for both the samples is calculated to be 4.2 μ_B/f.u., whereas theoretical saturation magnetic moment (μ_{sat}^{th}) is 3.3 μ_B/f.u. The experimental magnetic moment (μ_{sat}^{exp}) obtained for Sample A is 3.18 μ_B/f.u. which is very close to μ_{sat}^{th} value. For Sample B, the obtained value of μ_{sat}^{exp} is 2.81 μ_B/f.u. This low magnetic moment of Sample B may be due to the mixed magnetic phases or any canted magnetic phase present in the system at
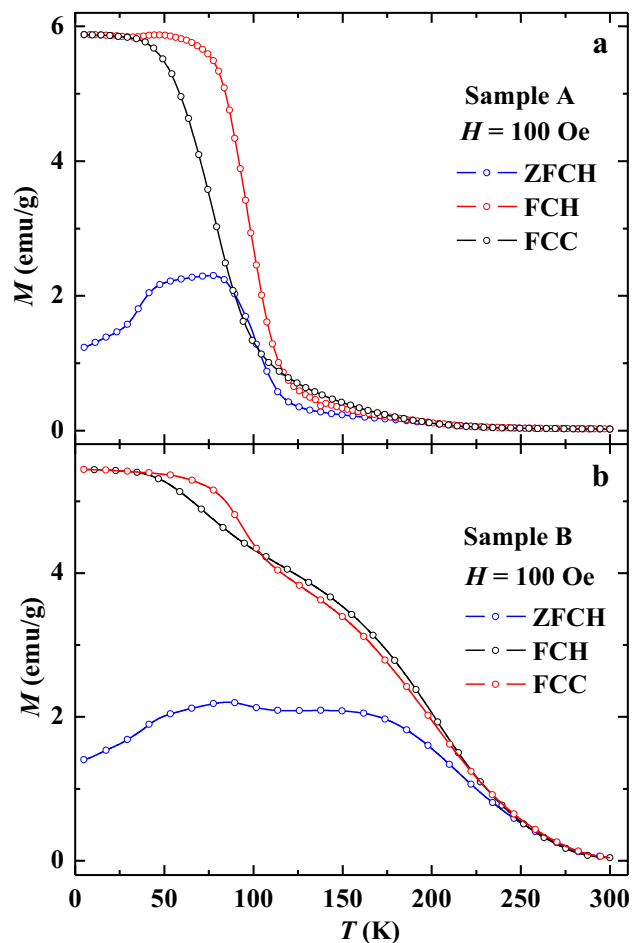

Figure 4. Magnetic moment (M) as a function of temperature (T) measured in zero-field-cooled heating (ZFCH), field-cooled heating (FCH) and field-cooled cooling (FCC) protocols in an applied field of 100 Oe for (**a**) Sample A and (**b**) Sample B.

low temperature. In the PM region using Curie-Weiss analysis, the experimental effective PM moment (μ_{exp}^{eff}) obtained are 4.43 μ_B/f.u. for sample A and 4.82 μ_B/f.u. for sample B. The larger values of effective magnetic moment of the samples further indicate a probable existence of FM cluster in the system.

To shed more light on the magnetic character of the studied samples at different temperature regions, we recorded isothermal variation of dc magnetization as a function of applied magnetic field at different constant temperatures (see figure 5a and d). Linear behaviour of $M(H)$ data for both the compounds indicate the PM nature of the compounds at room temperature. Around 130 K, the FM phase starts to dominate the behaviour of Sample A and a signature of field-induced growth of FM component is visible in the inset of figure 5a. At 80 and 10 K for Sample A, M shows initial rise with H accompanying field hysteresis, but does not saturate at 5 T (figure 5a). This clearly indicates the existence of an AFM component in the system. Similar M–H behaviour was also observed for Sample B at 100 and 5 K (figure 5d). As the

temperature is lowered (down to 5 K), the hysteresis becomes more and more prominent still coercivity remains negligible (≈100 Oe). As seen in figure 5b and c for Sample A and figure 5e and f for Sample B, the initial isothermal magnetization data does not trace the same path (virgin) on the subsequent field cycle indicating that the sample has been arrested in a soft FM state, which is retained in the subsequent return leg (indicated by arrow). The original homogeneous magnetic state transforms into inhomogeneous state and shows phase coexistence even at zero field. This type of field-induced phenomena or kinetic arrest is connected to the metastability of the system [23] and is also observed in other half-doped manganites [24]. The magnetization isotherm at 10 K (figure 5b) or at 5 K (figure 5e) may provide some more information on the nature of spin of AFM state with some AFM state changing near ≈1 T and some changing at ≈2 T (corresponding to harder spin) to FM state for Sample A (and ≈1.5 T and ≈3.5 T for Sample B). However, the absence of hysteresis in 3rd quadrant for both the samples at low temperatures (10/5 K) is the

signature of strong spin arrest with more dominance of FM state with respect to AFM. At higher temperatures (80 K for Sample A and 100 K for Sample B) different spin dynamic feature is observed, which shows hysteresis both on 1st and 3rd quadrant with zero coercivity, indicating the weakening of AFM state. Moreover, the subsequent field-decreasing (red curve) and field-increasing (blue curve) paths do not overlap (unlike at 10/5 K) as shown in figure 5c and f. For Sample A at 80 K (figure 5c), the subsequent field increasing line initially overlap with field reduced path up to ∼0.3 T followed by a crossover ∼0.9 T and for further increasing the field, it coincides with virgin curve at ∼1.7 T. However, at 100 K for Sample B, the subsequent increasing line coincides with virgin line for the entire measuring range of magnetic field. This difference in magnetization behaviour reflects the relative difference in inhomogeneous AFM-FM components present in the systems.

This complex magnetization dynamics was therefore studied for both the samples from low temperature up to 65 K,
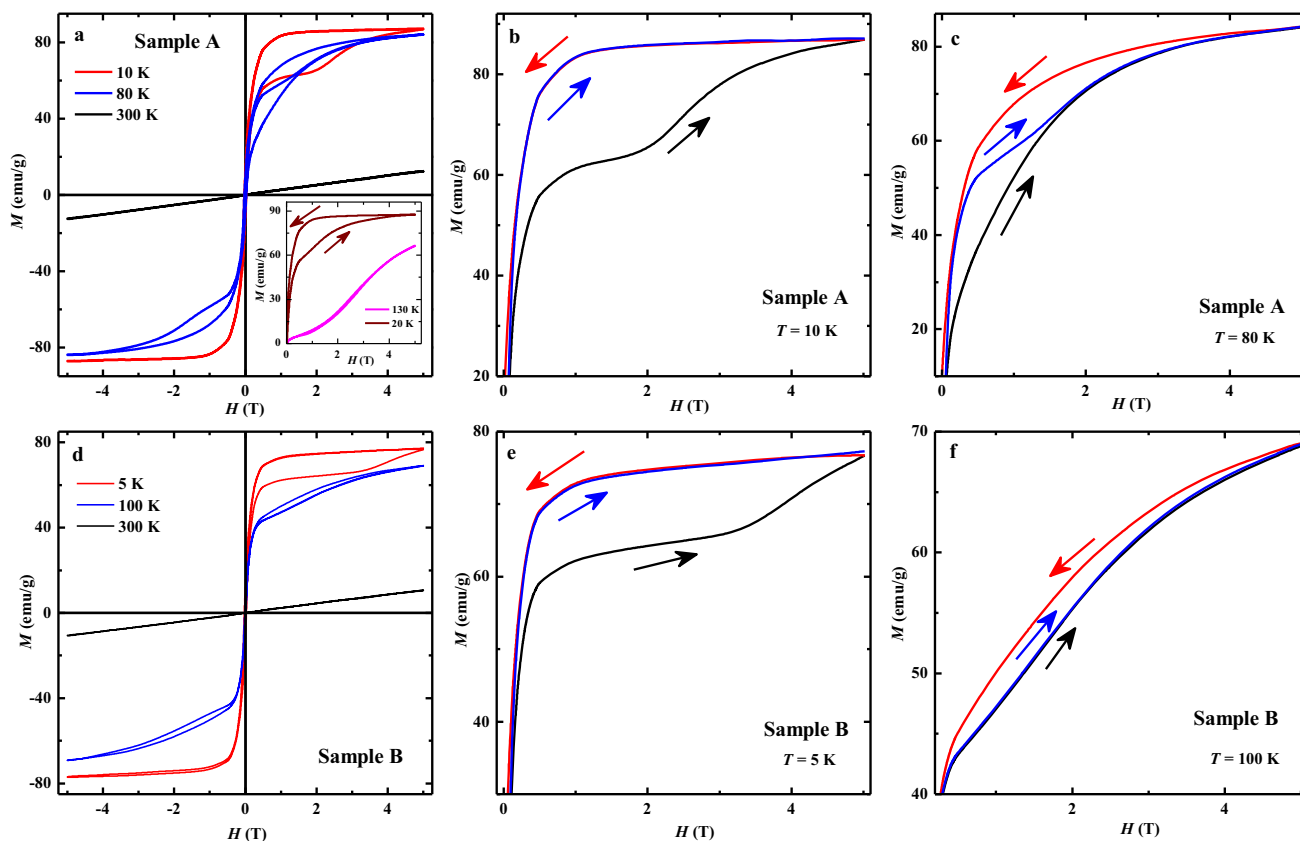

Figure 5. (**a**) Isothermal magnetization (*M*) of Sample A is plotted as a function of applied magnetic field (*H*) at different constant temperatures. The inset of (**a**) exhibits the extended view of the same for Sample A. (**b**) *M vs. H* of Sample A at 10 K. After reaching the highest field, the magnetization of the field-reducing path shows a complete overlap with the subsequent field-increasing path. (**c**) The initial or virgin *M vs. H* curve of Sample A at 80 K shows decrease in the field (∼1.5 T) of the AF to FM conversion. The subsequent field-decreasing and field-increasing paths (which define the envelope curve) do not overlap (unlike at 10 K) but lie above the virgin curve. (**d**) *M vs. H* of Sample B at different constant temperatures. (**e**) *M vs. H* of Sample B at 5 K. After reaching the highest field, the magnetization of the field reducing path shows a complete overlap with the subsequent field-increasing path. (**f**) *M vs. H* of Sample B at 100 K. The subsequent field-decreasing and field-increasing paths do not overlap but field-increasing path coincide with the virgin curve.
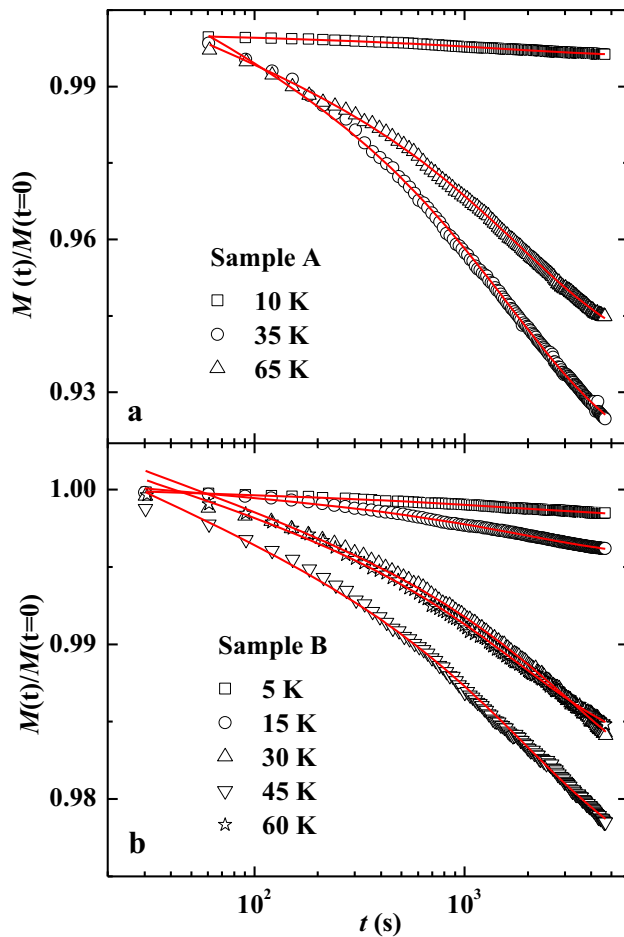
Figure 6. Isothermal magnetizations for (**a**) Sample A and (**b**) Sample B are plotted as a function of time (t) at different temperatures (T). Samples were first cooled in the presence of 50 Oe of applied field from 300 K to desired temperatures and M was measured as a function of t after removing external magnetic field.

where magnetic hysteresis is very strong. The sample was cooled down from 300 K to the desired temperature in 50 Oe field and time dependence of remnant magnetization was recorded just after the magnetic field is cutoff. The relaxation of remnant magnetization obtained experimentally is finally fit with the equation:

$$M(T) = M_0 + A_D \exp(-t/\tau) + A_L \ln(t), \qquad (1)$$

where M_0 is the FM component, 2nd term represents Debye relaxation process associated with activation against a single energy barrier, 3rd term represents the relaxation mechanism involved with the distribution of energy barriers or time-dependent activation energies usually obtained in disordered magnetic phase, τ represents the time constant in exponential relaxation process. Figure 6a and b shows the experimental data and corresponding fitting curve using equation (1). The result of this simulation is given in table 2. As obtained, both for Samples A and B, the weight factors (A_D and A_L) and

Table 2. Different fitting parameters of equation (1).

T (K)	A_D	A_L	τ (s)
Sample A			
10	1.034×10^{-04}	2.66×10^{-05}	1550.6
35	2.113×10^{-03}	4.97×10^{-04}	1624.3
65	1.253×10^{-03}	3.15×10^{-04}	1807.7
Sample B			
5	3.75×10^{-03}	1.34×10^{-03}	1790.4
15	1.18×10^{-02}	3.23×10^{-03}	1883.7
30	5.06×10^{-02}	1.20×10^{-02}	1910.5
45	5.36×10^{-02}	1.58×10^{-02}	1971.2
60	3.89×10^{-02}	1.02×10^{-02}	1780.7

time constant (τ) are showing a systematic increase in value with increasing temperature and then shows the decrease in value with further increase in temperature ($\geq$60 K), thus signifying the appearance of more disordered magnetic phase in the system. The presence of both Debye process and logarithmic relaxation as well as corresponding values of A_D, A_L and τ only reflects the presence of inherent magnetic disorder in both the systems. It is also interesting to see from table 2 that the value of A_D is one-order of magnitude higher in Sample B compared to Sample A, whereas value of A_L is two-order of magnitude higher for the same. These values are also useful in understanding the disorder in magnetization data (figures 4 and 5), suggesting that the nature of magnetic disorder in Sample B is much higher compared to that in Sample A in a quantitative way as influenced by inhomogeneous chemical distribution through extra heat treatment.

The variations of resistivity (ρ) as a function of temperature for both Samples A and B are shown in figure 7a and b, respectively. The measurement protocol for Sample A (and Sample B) is done during heating and subsequent cooling at cooling field $H_{cool} = 0$ T and at cycling field $H_C = 0$ T for blue curve in figure 7a. The red curve in figure 7a was obtained by using same protocol when $H_{cool} = H_C = 6$ T. The green one was obtained in heating cycle at 0 T ($= H_C$) field after cooling the sample at 5 T ($= H_{cool}$) and subsequent cooling curve was obtained at same value of H_C only as shown in figure 7a. Both zero field (blue curve) and 6 T field (red curve) data show diffuse insulator–metal behaviour and are associated with clear thermal hysteresis below ~100 and ~135 K, respectively, which again confirms the first-order nature of insulator–metal transition in Sample A. In addition, the resistivity of this sample decreases with magnetic field below ~100 K; i.e., negative magnetoresistance (MR) exists in the system. As the sample shows the field-induced transition, where external field destroys the AFM state and FM state sets in the system (figure 4a), the negative MR also comes out as a consequence of this change-over of AFM to FM state which is already known for some half-doped manganites [25]. As this negative MR is present in the system even much below the zone of thermal hysteresis, it
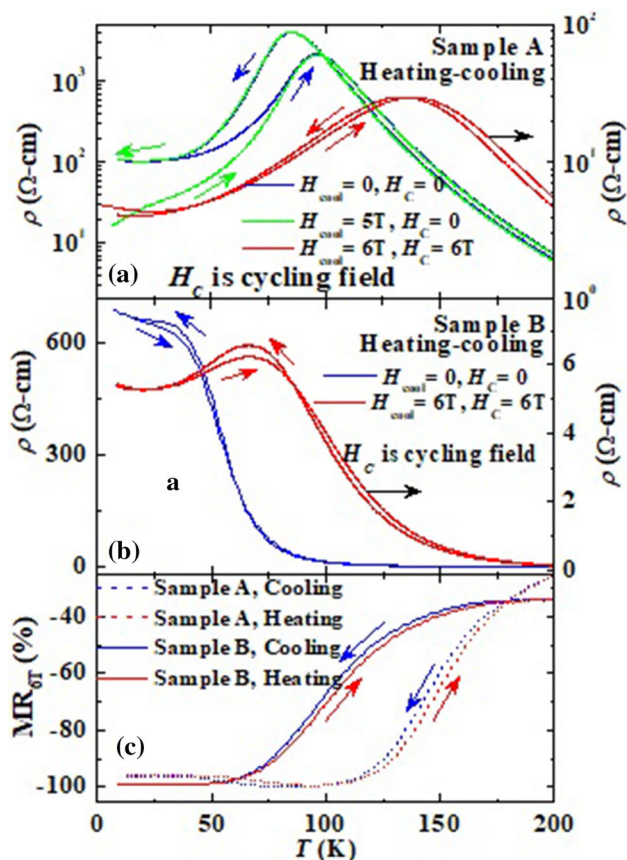
Figure 7. (**a**) Resistivity (ρ) as a function of temperature (T) is plotted for Sample A during heating and subsequent cooling sequences by blue curve: cooling field (H_{cool}) = 0 and cycling field (H_C = 0); green curve: H_{cool} = 5 T and H_C = 0; red curve: H_{cool} = 6 T and H_C = 6 T. (**b**) $\rho(T)$ behaviour of Sample B is shown during cooling and subsequent heating sequences by blue curve: H_{cool} = 0 T and H_C = 0 T; red curve: H_{cool} = 6 T and H_C = 6 T. (**c**) MR as a function of temperature for cooling and heating cycles for H = 6 T. Arrows indicate the direction of temperature change.

indicates some more factors responsible for this negative MR in the system apart from this AFM to FM change-over in it. In order to understand it, we need to look at the heating curve at H_{cool} = 5 T and H_C = 0 T (green curve), which shows the continuous decrease of resistance down to lowest temperature that corresponds to progressive arrest of field-induced FM state in the system. The green curve merges with H_{cool} = 0 T curve (blue curve) just above ~100 K, signifying that the field-induced arrest of FM state is connected with disorder-induced first-order phase transition in the system. For Sample A, the experimental data of magnetization (figure 4a) and resistivity (figure 7a) show the existence of PM insulating phase changing over to FM metallic phase at T_C. The striking difference is obtained for Sample B giving no metal-insulator transition below 30 K under zero field (blue curve) followed by a signature of slope change with small thermal hysteresis

below 30 K in $\rho(T)$ (figure 7b), which under a field of 6 T (red curve), shows field-induced metal-insulator transition at ~65 K in the same region in magnetization (figure 4b) with prominent thermal hysteresis. Temperature-dependent MR [= $(\rho(H) - \rho(H = 0))/\rho(H = 0)$] of both the samples are shown in figure 7c for both heating and cooling legs at 6 T field. MR behaviour closely resembles the resistivity behaviour of these samples (figure 7a and b) giving the MR minima (−99.2%) near the metal-insulator transition temperature at ~100 K for Sample A, which is reduced in value (approximately −96%) as the temperature is lowered. MR for Sample B on the other hand did not show any such minima and reached to lowest MR value (approximately −99.5%) near the metal-insulator transition temperature ~40 K and maintained this value to lowest temperature achieved. This correlation along with the difference in resistivity behaviour between the samples is following the same argument of inhomogeneous ionic distribution-mediated modification of their structure in atomic level changing the nature of lattice strain, thus showing the disorder dynamics between them.

4. Conclusions

Polycrystalline $Eu_{0.2}La_{0.3}Sr_{0.2}Ca_{0.3}MnO_3$ batch integrated sample is specially modified to introduce the difference in ionic distribution in its structure without modifying it in micro-level (grains). The orthorhombic structure with *Pnma* space group for both the samples shows atomic level modification, finally leading to opposite nature of strain ($OS_\perp$) along *b*-axis. The high negative value of $OS_\perp$ in Sample B indicates a probable de-stabilization of CO state in this system. The detailed magnetization behaviour as well as resistivity behaviour of both the samples proved this effect of modification of strain in the structure. The disorder (chemical) due to the coexistence of divalent Sr and Ca and trivalent Eu and La, can destroy charge ordering in half-doped manganite system. With inhomogeneity of ionic distribution, the situation becomes complicated as the system will try to balance between many factors, such as more Mn^{3+}/Mn^{4+} ratio, unit cell volume decrease (table 1), tolerance factor, charge ordering, etc. It may be possible that comparatively homogeneous ionic distribution help to retain charge ordering in Sample A and thus first-order transition is involved. This study therefore shows the tuning of de-stabilization of CO state in half-doped manganites by introducing the structural disorder through different ionic distribution in polycrystalline sample.

References

[1] Kuwahara H, Tomioka Y, Asamitsu A, Moritomo Y and Tokura Y 1995 *Science* **270** 961

[2] Tomioka Y, Asamitsu A, Kuwahara H, Moritomo Y and Tokura Y 1996 *Phys. Rev. B* **53** R1689

[3] Asamitsu A, Tomioka Y, Kuwahara H and Tokura Y 1997 *Nature(London)* **388** 50

[4] Kimura T, Tomioka Y, Kumai R, Okimoto Y and Tokura Y 1999 *Phys. Rev. Lett.* **83** 3940

[5] Kozlenko D P, Jirák Z, Goncharenko I N and Savenko B N 2004 *J. Phys. Condens. Matter* **16** 5883

[6] Rao S S, Anuradha K N, Sarangi S and Bhat S V 2005 *Appl. Phys. Lett.* **87** 182503

[7] Sarkar T, Mukhopadhyay P K, Raychaudhuri A K and Banerjee S 2007 *J. Appl. Phys.* **101** 124307

[8] Sarkar T, Raychaudhuri A K and Chatterji T 2008 *Appl. Phys. Lett.* **92** 123104

[9] Sarkar T, Raychaudhuri A K and Chatterji T 2008 *Phys. Rev. B* **77** 235112

[10] Das H, Sangiovanni G, Valli A, Held K and Saha-Dasgupta T 2011 *Phys. Rev. Lett.* **107** 197202

[11] Gutiérrez D, Radaelli G, Sanchez F, Bertacco R and Fontcuberta J 2014 *Phys. Rev.* **89** 075107

[12] Chaddah P, Kumar K and Banerjee A 2008 *Phys. Rev. B* **77** 100402(R)

[13] Chatterjee S, Giri S and Majumdar S 2010 *J. Appl. Phys.* **107** 113909

[14] Giri S K and Nath T K 2011 *J. Nanosci. Nanotechnol.* **11** 4806

[15] Pramanik A K and Banerjee A 2010 *Phys. Rev. B* **82** 094402

[16] Jirák Z, Hadová E, Kaman O, Knížek K, Maryško M, Pollert E, *et al* 2010 *Phys. Rev. B* **81** 024403

[17] Auslender M, Shames A I, Rozenberg E, Sominski E, Gedanken A and Mukovski Y M 2010 *J. Appl. Phys.* **107** 09D702

[18] Rozenberg E, Tsindlekht M I, Felner I, Sominski E, Gedanken A, Mukovskii Y M *et al* 2009 *IEEE Trans. Magn.* **45** 2576

[19] Markovich V and Jung G 2012 *Phys. Rev. Lett.* **108** 129701

[20] De K, Ray R, Panda R N, Giri S, Nakamura H and Kohara T 2005 *J. Magn. Magn. Mater.* **288** 339

[21] Lutterotti L, Matthies S and Wenk H R 1997 *J. Appl. Phys.* **81** 594

[22] Shankar U and Singh A K 2015 *J. Phys. Chem. C* **119** 28620

[23] Sethna J P, Dehmen K, Kartha S, Krumhans J A, Roberts B W and Shore J D 1993 *Phys. Rev. Lett.* **70** 3347

[24] Banerjee A, Pramanik A K, Kumar K and Chaddah P 2006 *J. Phys. Condens. Matter* **18** L605

[25] Chatterjee S, Giri S and Majumdar S 2012 *J. Phys. Condens. Matter* **24** 366001